Article:
Yang, J. orcid.org/0000-0003-4161-8379, Chen, X., Lin, J. et al. (5 more authors) (2024) Co-delivery of resveratrol and curcumin based on Mesona chinensis polysaccharides/zein nanoparticle for targeted alleviation of ulcerative colitis. Food Bioscience, 59. 104060. ISSN 2212-4292

https://doi.org/10.1016/j.fbio.2024.104060

Co-delivery of resveratrol and curcumin based on *Mesona chinensis* polysaccharides/zein nanoparticle for targeted alleviation of ulcerative colitis

Jun Yang[a, b], Xianxiang Chen[a], Jieqiong Lin[a], Mingyue Shen[a], Yuanxing Wang[a], Anwesha Sarkar[b, *], Huiliang Wen[a], Jianhua Xie[a, *]

[a] *State Key Laboratory of Food Science and Resources, Nanchang University, Nanchang 330047, China*

[b] *Food Colloids and Bioprocessing Group, School of Food Science and Nutrition, University of Leeds, Leeds, LS2 9JT, United Kingdom*

*Corresponding authors, address at State Key Laboratory of Food Science and Resources, Nanchang University, No. 235 Nanjing East Road, Nanchang 330047, Jiangxi, China

Tel: +86-791-88304347; Fax: +86-791-88304347

E-mail address: A.Sarkar@leeds.ac.uk (A. Sarkar), jhxie@ncu.edu.cn (J. Xie)

15 **Graphical abstract**

16

17

18

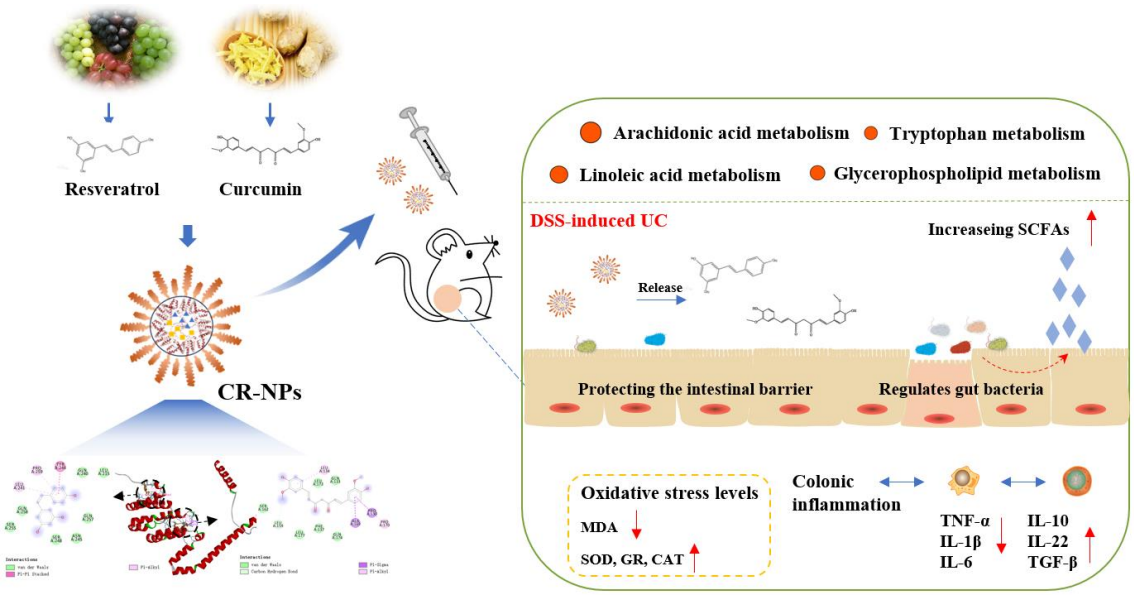

Highlights

- Nanoparticles prepared by MCP and zein can effectively co-encapsulate curcumin and resveratrol.
- Favorable gastrointestinal stability of nanoparticles prepared based on the water evaporation cross-linking.
- Co-delivery of curcumin and resveratrol can effectively alleviate the symptoms of ulcerative colitis.
- CR-NPs maintained the balance of intestinal flora and promoted the production of short-chain fatty acids.
- CR-NPs alleviate UC by modulating arachidonic acid, linoleic acid, and tryptophan metabolism.

Abstract

Herein, a novel oral nano-delivery system (CR-NPs) was designed for co-delivering curcumin and resveratrol to treat ulcerative colitis (UC) using *Mesona chinensis* polysaccharides and zein via antisolvent precipitation and continuous water evaporation crosslinking. It showed high encapsulation rates for both bioactives due to hydrogen bonding and hydrophobic forces. CR-NPs have favorable *in vitro* gastrointestinal stability and low pre-colonic release rates, resulting in increased accumulation in the colon. *In vivo* therapeutic effects of CR-NPs were confirmed through alleviation of UC symptoms and inflammation of UC mice. CR-NPs maintained the balance of intestinal flora and promoted the production of short-chain fatty acids in UC mice. Furthermore, CR-NPs intervention can alleviate the development of UC by modulating arachidonic acid, linoleic acid, and tryptophan metabolism. This study provides some theoretical basis using a novel dietary protocol option that co-delivering natural bioactives to the colon for alleviation of UC.

Keywords: Nanoparticle; Protein; Polysaccharides; Nanosystem; Inflammation

1. Introduction

Ulcerative colitis (UC) is a type of inflammatory bowel disease that causes abdominal pain, bloody diarrhea, weight loss, and even may trigger cancer. The main causes for the development of UC are genetic predisposition, dietary patterns and associated gut microbiota, and other external environmental stimuli (Du & Ha, 2020). The incidence of UC is high with nearly 5 million cases

49 predicted the globe in 2023, and it is clinically difficult to cure UC completely (Kaplan, 2015). The
50 main clinical drugs used are 5-aminosalicylic acid and corticosteroids drug. However, the financial
51 burden, side effects, and drug resistance of long-term medication offer severe clinical challenges for
52 UC patients (Naeem et al., 2020). The efficacy of these non-targeted drugs is often limited and short-
53 lived, so new low-cost, efficient, biocompatible, and non-toxic treatment strategies are in pressing
54 need to bring therapeutic breakthroughs for UC treatment. Consequently, there has been a
55 burgeoning interest in administering food-grade bioactives using various encapsulation strategies as
56 alternative routes to typical single drug administration approach to address UC (do Nascimento et
57 al., 2020). Among these, the small size of nanoparticles allows for larger contact area with the
58 intestinal mucosa, which has a higher gastrointestinal residence time and promotes the accumulation
59 and uptake of the bioactives in the gastrointestinal tract (Yang et al., 2021). In recent years, a variety
60 of carrier forms (*e.g.*, hydrogels, emulsions, liposomes, nanoparticles) have been used to deliver
61 food-grade bioactives (e.g., resveratrol, anthocyanins, curcumin, quercetin, tea polyphenols) to
62 improve their chemical stability and bioavailability at site of action (Araiza-Calahorra et al., 2018;
63 Wu et al., 2023). Such biocompatible delivery approaches for nutraceuticals promise to allow
64 personalized nutrition and disease prevention and alleviation (Nedovic et al., 2011). It is noteworthy
65 although often single nutrients are used in clinical settings, single nutrients are rarely consumed. In
66 addition, the synergistic interaction between combinatorial nutrients may result in better activity
67 compared to single ingredients, although remains poorly understood (de Kok et al., 2008). The
68 combined intake of multiple bioactives also avoids the potential side effects and toxicity of high

concentrations of a single nutraceutical. Thus, co-delivery systems have been a preferred choice to enhance pharmacokinetic behaviour and achieve site-targeting delivery.

Curcumin is a naturally occurring bioactive polyphenol with a diketone structure extracted from turmeric and is one of the most heavily researched phytochemicals used in the colour, fragrance, skin care, and dietary supplement industries. Curcumin has anti-inflammatory, antibacterial, antioxidant, and other biological activities which are considered to be safe for human consumption as an active food ingredient (Esatbeyoglu et al., 2012). Resveratrol on the other hand is also an active polyphenol found in a wide variety of fruits, especially grapes, and red wine. It is widely known for its anti-inflammatory, antioxidant, and cardiovascular health maintenance activities (Jinglin Zhang et al., 2023; Yang et al., 2024). Curcumin and resveratrol have been individually reported to play a pivotal role in alleviating the symptoms of UC and maintaining intestinal function due to their antioxidant and anti-inflammatory activities (Ma et al., 2022). Moreover, several studies have shown synergistic interactions between curcumin and resveratrol in terms of antioxidant activity, anti-inflammatory, and anti-cancer activity (Aftab & Vieira, 2010).

However, the poor water solubility, oxidative degradation, and low bioavailability of polyphenolic compounds limit their widespread application (Nunes et al., 2018). Encapsulating them in a nano-delivery vehicle can effectively alleviate these challenges, and nano-delivery vehicles prepared from natural polysaccharides and proteins are of great interests due to their good biocompatibility, non-toxicity, biodegradable properties, low cost, high encapsulation rate, and targeted delivery capability (Yang et al., 2020). Zein, a plant protein with favorable self-assembling

89 properties, has been widely reported to be used for the encapsulation of hydrophobic substances.
90 However, zein is susceptible to proteases in the gastrointestinal tract, thus surface modifications
91 with polysaccharides are required to improve its stability (Yuan et al., 2022). *Mesona chinensis*
92 polysaccharide (MCP) is an acidic heteropolysaccharide derived from *Mesona chinensis* Benth. It
93 has excellent rheological, gelation properties and bioactivity, and shown to be suitable for the
94 development of a variety of delivery systems such as hydrogels and emulsions (Pan et al., 2024).
95 Co-encapsulation of curcumin and resveratrol in polymeric emulsion systems has been reported to
96 improve their stability and bioaccessibility (Liu et al., 2018). However, there are no reports on co-
97 encapsulated curcumin and resveratrol in nano-delivery systems and applied to nutritional
98 interventions in UC.

99 The onset of UC is usually in the colon and rectum, which requires nanocarriers that can
100 survive the entire gastrointestinal environment across a wide range of pH challenges and then allow
101 delivery of the actives to the colon. Current protein-based carriers are generally susceptible to
102 degradation by digestive enzymes, which may lead to early leakage of the actives. Surface coating
103 with polysaccharides can improve their stability in the gastrointestinal environment (Yuan et al.,
104 2022). Nevertheless, enhancing the gastrointestinal stability of these proteinaceous nanoparticles
105 encapsulating bioactives by optimising their surface has been given little attention to date, despite
106 it is importance for colon-targeted delivery. Especially, the cross-linkable sites on the polysaccharide
107 and protein chains are limited and the inactive interaction sites can only be partially activated (Wang
108 et al., 2019). Therefore, it is of interest to increase the efficiency of the surface coating for the

109 stabilization of protein nanoparticles to prevent them from being biologically degraded by digestive
110 enzymes to allow releasing the actives in the colon to address UC (Doublier et al., 2000). In the
111 traditional Chinese "Simmering soup" diet, it has been found that various food ingredients can end
112 up in a rich "Soup stock" during the continuous free evaporation of water. This implies that higher
113 intensity cross-linking of the polymer may be promoted during the continuous evaporation of water.
114 Inspired by this traditional diet design, our study designs a novel protein-polysaccharide based nano
115 vehicle to co-deliver curcumin and resveratrol in the colon to address UC.

116 Herein, a novel oral co-delivery nano-system was developed based on *Mesona chinensis*
117 polysaccharides and zein with the assistance of water evaporation-based crosslinking. The enhanced
118 permeation retention effect would passively target nanoparticles to reach the inflamed region,
119 provided that the nanoparticles are not disrupted by the gastrointestinal environment (Hu et al.,
120 2020). In this study, it was hypothesized that a facile cross-linking process *via* water evaporation
121 could increase the *in vitro* gastrointestinal stability of MCP-zein nanoparticles while co-delivering
122 curcumin and resveratrol targeting to the inflamed mucosa. The therapeutic efficacy of co-delivery
123 of curcumin and resveratrol for UC was subsequently assessed *in vivo* in mice by UC symptoms,
124 intestinal mucosal function, inflammatory factor release, oxidative stress levels, intestinal flora, and
125 the content of short-chain fatty acids. To our knowledge, there are no reports on the treatment of UC
126 with curcumin and resveratrol co-delivery systems using nano-biopolymeric delivery vehicles,
127 especially based on water evaporation cross-linking method. This study provides a theoretical basis
128 for the development of nutrition intervention strategies for the oral co-delivery of food bioactives

129 in UC and inflammatory bowel disease.

130 **2. Material and method**

131 *2.1 Material*

132 Resveratrol (99% purity) was purchased from Aladdin (Shanghai, China). Curcumin (98%
133 purity) and zein were purchased from Adamas (Shanghai, China). Pepsin (≥400 units/mg) and 5-
134 aminosalicylic acid (ASA) were purchased from Sigma Aldrich (Shanghai, China). Trypsin (>250
135 U/mg) was purchased from Solarbio (Beijing, China). Bile salts of porcine origin were purchased
136 from Macklin (Shanghai, China). Dextran sulfate sodium (DSS) was obtained from MP Biomedicals
137 (Santa Ana, California, USA). Tumour necrosis factor-α (TNF-α), interleukin-1β (IL-1β),
138 interleukin-6 (IL-6), interleukin-10 (IL-10), and interleukin-22 (IL-22) kits were obtained from
139 Boster Biological Technology (Wuhan, Hubei, China). Bicinchoninic Acid (BCA), 3,4-
140 Methylenedioxyamphetamine (MDA), Superoxide Dismutase (SOD), Glutathione reductase (GR),
141 and Catalase (CAT) kits were obtained from Beyotime Biotechnology (Shanghai, China). Endotoxin
142 (ET) and lipopolysaccharide binding protein (LBP) kits were purchased from Shanghai Enzyme
143 Link Reagent Company (Shanghai, China). All other reagents were of analytical grade.

144 *2.2 Extraction and structural characterization of MCP*

145 *Mesona chinensis* polysaccharides (MCP) were extracted from *Mesona chinesis* Benth by hot
146 water with the addition of sodium carbonate. Briefly, fresh *Mesona chinesis* Benth (Xiaoshicheng,
147 Jiangxi, China) was sun-dried, soaked in 80% ethanol overnight at 25 ℃, and then ethanol was

evaporated. MCP was extracted with hot water (1:15, 95 °C, 2 h) added with 5% sodium carbonate. The above steps were repeated three times for the filtrate, and the supernatant was collected and combined, concentrated to a certain volume, and then precipitated with 80% ethanol overnight. The precipitate was collected and dissolved in ultrapure water, and the solution was used to remove proteins by Sevage method. After 48 h of dialysis, the solution was freeze-dried. The lyophilized powder was resuspended in ultrapure water and centrifuged (5,795×g, 15 min) to remove the precipitate, 30% ethanol was added to precipitate it overnight. The supernatant was then collected and precipitated again with 70% ethanol overnight, and the precipitate was collected for re-dispersion, concentration, dialysis, and then was lyophilized to obtain the MCP powder.

The uronic acid, neutral sugar, and protein content of MCP were determined by the carbazole-sulphuric acid method, phenol-sulphuric acid method, and Coomassie Brilliant Blue method, respectively (Yang et al., 2022). The distribution of the relative molecular mass of MCP was determined by high performance gel permeation chromatography (HPGPC, Agilent, USA). The relative molecular mass of MCP was calculated from the curve between the retention time of HPGPC and the relative molecular mass of standard dextran. The monosaccharide composition of MCP was determined by sulfuric acid hydrolysis (12 M, 110 °C, 3 h) followed by ion chromatography (ICS5000, USA). The 1D and 2D nuclear magnetic resonance (NMR) of the MCP was determined using an NMR spectrometer (Bruker AV 600 MHz, Switzerland). Briefly, MCP was dissolved in deuterium oxide, and after three consecutive deuterium exchanges of the polysaccharide using a lyophilizer, MCP was dissolved in 0.5 mL of deuterium oxide and the 1H

NMR, Correlated spectroscopy (COSY), heteronuclear single quantum coherence (HSQC), total correlation spectroscopy (TOCSY), and heteronuclear multiple bond correlation (HMBC) of MCP were recorded at 25 ℃.

2.3 Preparation of CR-NPs

A suitable amount of zein was weighed and dissolved in 75%-80% ethanol aqueous solution to prepare a 20 mg/mL zein stock solution. Curcumin (Cur, 1 mg/mL) and resveratrol (Res, 1 mg/mL) were dissolved in advance into the zein solution. An appropriate amount of MCP power was weighed and dissolved in ultrapure water to form a 1 mg/mL MCP stock solution. The zein mixture solution was rapidly injected into the MCP solution (1:10 (v/v)) using a disposable syringe under a 55 °C water bath and magnetic stirring to form zein polysaccharide/zein mixture particle solution. The mixed particle solution standing in a water bath at 55 °C for 10 min was then transferred to a rotary evaporator preheated in advance (55 °C), where the mixed particle solution was continuously cross-linked for 2-3 h under constant evaporation of water, and the finally obtained nanoparticles containing both Cur and Res were named as CR-NPs. As a control, only antisolvent based MCP/zein nanoparticles (AS-ZMNPs) and zein NPs without the continuous evaporation-based crosslinking step was also fabricated to understand the benefit of the adding water evaporation step on the creation of these unique nano-delivery vehicles.

2.4 Characterization of CR-NPs

The particle size and zeta potential of freshly prepared CR-NPs samples without dilution were

187 determined using a Malvern Zetasizer (Malvern, Worcestershire, UK) *via* dynamic light scattering
188 (DLS). The microstructure of CR-NPs was observed by transmission electron microscopy (TEM,
189 HT7800/HT7700, Japan). The encapsulation rate of CR-NPs was determined by first extracting Cur
190 and Res by 80% ethanol and then measuring the absorbance values at 426 nm and 306 nm with an
191 Thermo Scientific Varioskan Flash (Thermo, USA), and the encapsulation was calculated using a
192 standard curve made in advance. Fourier transform infrared spectroscopy (FTIR, Nicolet 5700, USA)
193 and X-ray diffraction (XRD, D8 Advance, Bruker, Germany) were used for the determination of the
194 chemical and crystalline structures of the CR-NPs powders.

195 *2.5 In vitro digestibility and release*

196 For *in vitro* digestion experiments, 10 mL of samples were digested with an equal volume of
197 simulated gastric fluid (SGF, 4.2 mg/mL NaCl, 2000 U/mL pepsin, pH 2) at 37 °C, 200 rpm for 2 h.
198 Then, the pH was immediately adjusted to neutral and 10 mL of simulated intestinal fluid (SIF, 4.48
199 mg/mL bile salts, 100 U/mL trypsin, pH 7.2) was added at 37 °C, 200 rpm for 4 h (Minekus et al.,
200 2014). The fluids from the simulated gastric and intestinal digestion phases were collected
201 separately for sodium-dodecyl sulphate polyacrylamide gel electrophoresis (SDS-PAGE) analysis.
202 Briefly, the CR-NPs samples were added to the loading buffer, denatured at 95 °C for 5 min, then
203 20 μL all samples were subjected to SDS electrophoresis (80 V, 25 min, 120 V, 1 h), and at the end
204 of the process, stained with Coomassie Brilliant Blue and visualized in a gel imaging system (BIO-
205 RAD, USA). The soluble peptides were determined according to a previous method (Yan et al.,
206 2021). The digested samples were added with an equal volume of 10% trichloroacetic acid, and after

half an hour, the supernatant was centrifuged and the content of soluble peptides in the supernatant was determined by BCA kit.

The *in vitro* release rate of Cur and Res from CR-NPs was determined according to the previously reported method with slight modifications (Anitha et al., 2011). Briefly, CR-NPs samples loaded with Cur and Res were dispersed in 0.01 M dilute hydrochloric acid solution (pH 2.0) for 2 h and then transferred to PBS buffer at pH 7.2 for 4 h. The samples were incubated in a constant temperature shaker (200 rpm, 37 °C). Considering the poor water solubility of Cur and Res, 0.05% Tween was added to all release media. The absorbance values were measured at fixed time intervals using a Thermo Scientific Varioskan Flash (Thermo, USA).

2.6 Molecular docking

Molecular docking was carried out to understand the interaction between nanoparticles and Cur/Res. The 3D molecular model of zein was downloaded from Uniprot website (https://www.uniprot.org), and the small molecule receptors such as Cur and Res were downloaded from Drugbank website (https://www.drugbank.ca). The individual files were converted into pdp format, and the receptors and ligands were subjected to hydrogenation, charge calculation, and other operations using Autodock software (version 1.5.7, Scripps), then imported into Pymol software (version 2.5.4, DeLano Scientific LLC) to construct the simulation box, and the molecular docking was carried out after determining the specific positional parameters, with the energy range set to 5 and the number of dockings set to 20. The results after docking were processed with Pymol software and Discovery studio (version 4.5, BIOVIA) for interaction force analysis.

227 *2.7 In vivo therapeutic effect of CR-NPs against UC*

228 Six-week-old C57BL/ 6 male mice weighing between 20-22 g were purchased from Hunan
229 SLAC Jingda Laboratory Animal Co., Ltd. and were randomly divided into four groups, control
230 group (healthy mice), model group (DSS-induced UC), positive group (5-aminosalicylic acid
231 treatment), and CR-NPs group (CR-NPs treatment) after one week of resting. At the end of the
232 resting period, mice were given CR-NPs (Cur and Res at 5 mg/kg) continuously for two weeks, and
233 at the end of the first week, the drinking water in the model, positive and CR-NPs groups was
234 replaced with water containing 3% DSS. Changes in body weight, blood in stool, and fecal hardness
235 were continuously recorded and scored as disease activity index (DAI). After decortication by
236 cervical dislocation, the blood, organ, and colonic tissues of mice were obtained and stored at -80 °C.
237 All animal experiments in this study followed the guidelines of the National Research Council's
238 Guide for the Care and Use of Laboratory Animals.

239 Terminal colon tissues were taken and placed in formalin fixative, embedded in paraffin, and
240 sectioned, and the samples were analyzed by H&E and AB-PAS staining. After homogenization of
241 the colon tissue, the content of inflammatory factors and cytokines (TNF-α, IL-1β, IL-6, IL-10, IL-
242 22, and TGF-β) in the supernatant was determined with the corresponding enzyme-linked
243 immunoassay kit. The levels of oxidative stress in mice were measured by measuring the levels of
244 MDA, SOD, GR, and CAT in liver tissue. The blood of mice was obtained, rested for 4 h and then
245 centrifuged to extract the serum. ET and LBP levels were determined by the kit on the serum.

246 *2.8 Analysis of intestinal flora and short-chain fatty acids*

Mouse feces are collected before sacrifice and stored at -80 °C for subsequent 16S rRNA analysis. The fecal samples were first extracted by DNA extraction using OMEGA Soil DNA Kit, then the molecular weight was determined by agarose gel electrophoresis, and the DNA was quantified by UV spectrophotometer. Different regions of the functional genes of the bacterial 16S rRNA gene were then amplified by PCR, and the PCR products were quantified using the Quant-iT PicoGreen dsDNA Assay Kit. Subsequently, Illumina's TruSeq Nano DNA LT Library Prep Kit was used for library construction, After the library was quality controlled and quantified, the qualified library was sequenced and analyzed. The analysis and visualization of the data is operated through an online platform (https://www.genescloud.cn).

After the mice were sacrificed, the contents of mouse cecum were collected, the appropriate amount of cecum contents was weighed and homogenized with physiological saline. Then the supernatant was centrifuged and passed through 0.22 μm aqueous filter head, 10% sulfuric acid was added and mixed, and the internal standard and anhydrous ether were added and centrifuged. The supernatant was passed through 0.22 μm organic filter head, and then short chain fatty acids (SCFAs) were determined by gas chromatography (Agilent 8890, USA) equipped with an HP-FFAP column (30 m×0.32 mm, 0.25 μm).

2.9. Metabolomics analysis

Serum sample (80 μL) was mixed according to 1:4 (*v/v*) with acetonitrile water (4:1, *v/v*) solution. Subsequently, it was centrifuged in a high-speed centrifuge (17,186×g, 12 min) at 4 °C. After centrifugation, the supernatant was taken, passed through a 0.22 μm organic filter membrane,

and transferred to the sample bottle. For mouse fecal samples, 80 mg of faces was weighed and mixed with organic extraction solvent (ultrapure water, methanol, and acetonitrile, 1:1:1, *v/v/v*). Subsequently, the sample was centrifuged at 17,186×g for 12 min and then the supernatant was passed through a 0.22 μm organic filter membrane into sample bottle. Each sample (10-15 μL) was aspirated into a separate sample bottle for quality control (QC). Samples were subsequently analyzed by UPLC-Q-TOF/MS. The chromatographic column was selected a C18 column (1.8 μm, 2.1 mm ×100 mm). The column temperature was maintained at 40 °C with an injection volume of 5 μL. The mobile phases were 0.1% formic acid aqueous solution and 0.1% formic acid acetonitrile in mobile phase A and B, respectively. The elution program was 0-3 min, 5%-16% B, 3-8 min, 16%-30% B, 8-10 min, 30%-52% B, 10-18 min, 52%-65% B, 18-26 min, 65%-100% B, 26-28 min, 100%-5%. The mass spectrometry conditions were as follows: the ion source was Dual ESI, and the ion modes were positive and negative ion modes, and the scanning range was set to 50-1200 m/z.

2.10. Statistical analysis

Experiments were repeated at least three times in this study and the dates were plotted and analyzed by using Origin and prism software. Data were compared for significance using t-test and one-way analysis of variance (ANOVA), and $p < 0.05$ was considered significant.

3. Results and discussion

3.1 Structural characterization of MCP

It was important to characterize MCP to understand its role in the fabrication of the nano-

delivery vehicle. After MCP extraction, its basic physicochemical properties were determined and it is a naturally occurring acidic polysaccharide composed mainly of 56.82% ± 1.02% uronic acid, 30.83% ± 1.66% neutral sugars, and 6.11% ± 0.64% proteins. MCP exhibits a major symmetry peak with a homogeneous distribution and has a molecular weight of approximately 1.83×10^5 Da (Fig. 1A). The monosaccharide composition of MCP is mainly galacturonic acid with rhamnose, arabinose, galactose, glucose, and glucuronic acid contributing to smaller proportions of the total composition (Fig. 1B). According to the monosaccharide composition and previous reports, it can hypothesize that MCP may possess a structure with a galacturonic acid as the main backbone with various sugar residues (Feng et al., 2008). MCP was further analyzed by 1D and 2D NMR. As shown in Fig. 1C, most of the isohead hydrogens of MCP were in the range of 5.0-5.5, suggesting that the galacturonic acid of the main chain was connected by α-glycosidic bond (Perrone et al., 2002). Two peaks were found at δ 1.12 and 1.16, which are signals for H of the methyl group on rhamnose, indicating the presence of at least two different positions of rhamnose. Additionally, there is a slight signal at δ 2.15, which may be attributed to the presence of a small amount of methoxyl groups (Tang et al., 2021).

The 1D H spectra and the heavily overlapping parts in combination with the 2D HSQC, COSY, HMBC, and TOCSY of the MCP corroborated to those in previous reports (Roger et al., 2004; Shakhmatov et al., 2015; Tang et al., 2021; Zhu et al., 2021). The strong signal at δ 5.32-5.39 may be attributed to H1 of α-1, 4-galacturonic acid, and Perrone et al. (2002) had reported a similar signal of H1 of α-1, 4-galacturonic acid between δ 5.3-5.4. The presence of distinct cross peaks of δ

306 5.39/3.65, 3.65/3.8, and 3.84/3.96 in the COSY spectrum (Fig. 1D) belong to H1-H2, H2-H3, and
307 H4-H5 of α-1, 4-galacturonic acid (Zhu et al., 2021). Also, strong signals were observed at δ
308 5.39/99.97, 3.65/71.82, 3.8/60.59, 3.84/71.6, and 3.96/73.21 in the HSQC spectrum, giving
309 chemical shifts of H1/C1-H5/C5 of α-1,4-galacturonic acid (Fig. 1E), which results are similar to
310 those reported by Petersen et al. (2008), who attributed it to α-1, 4-galacturonic acid. Therefore, we
311 confirm that the main backbone of MCP was composed of α-1, 4-galacturonic acid.

312 Moreover, a clearly differentiated H1 signal from α-1, 4-galacturonic acid at δ 5.33-5.35 was
313 found, which was speculated to be a possible case of branching in the main chain. Previous report
314 found that δ 5.33 and 3.95 were corresponding to H1 and H2 of α-(1, 2, 4)-D-GalpA (Shakhmatov
315 et al., 2015), and similar results were found in HMBC (Fig. 1F) and TOCSY spectrum (Fig. S1). We
316 therefore speculate that α-(1, 2, 4)-D-GalpA may exist. Also, α-L-Rhap was deduced from a
317 combination of δ 1.16 (H of CH_3) in ^{1}H NMR and δ 4.96/98.21 (H1/C1) chemical shifts in the
318 HSQC spectrum (Zhu et al., 2021). Both rhamnose residues including α-(1, 2, 4)-L-Rhap and α-1,2-
319 L-Rhap were identified. Moreover, some other residues such as β-D-Glcp and β-D-Galp were also
320 found. The coupled signals at δ 4.45/3.58 (H1-H2), 3.97/3.55 (H5-H6), 3.63/76.73 (H3/C3),
321 3.97/69.8 (H5/C5), and 4.45/3.63 (H1-H3) were found to belong to the β-D-Galp, whereas the
322 chemical shifts at δ 4.65 /3.26 (H1-H2), 3.26/3.54 (H2-H3), 3.54/3.39 (H3-H4), 3.39/68.87 (H3-C4)
323 belong to β-D-Glcp in the COSY, HSQC, and TOCSY spectra, respectively (Roger et al., 2004; Tang
324 et al., 2021). Therefore, MCP may also have α-(1, 2, 4)-L-Rhap, α-(1, 2)-L-Rhap, β-D-Galp, and β-
325 D-Glcp residues (Table S1). In the HMBC spectra, a coupling signal (δ 4.96/78.23) was found

between C2 of α-(1, 2, 4)-D-GalpA and H1 of α-L-Rhap, suggesting that the galacturonic acid of the main chain is linked to branched rhamnose via α-1, 2-glycosidic bond. Based on the monosaccharide composition, the theory of relative ordering of polysaccharide structures (Wang et al., 2021), and 1D/2D NMR results, combined with the previously reported rheological properties of MCP (Lin et al., 2018), MCP appears to be acidic heteropolysaccharide with a possible deduced structure of α-1, 4-GalpA as a backbone with some branched residues of α-L-Rhap.

3.2 Structural characteristics of CR-NPs

It is well known that antisolvent precipitation is a well-established method for the preparation of nanoparticles with a shell-core structure, and the preparation of CR-NPs was developed based on the antisolvent precipitation method followed by continuous water evaporation-based crosslinking. The average hydrodynamic particle size of CR-NPs was 179.83 ± 2.35 nm (Fig. 2A), and the zeta potential was -30.83 ± 0.74 mV (Fig. 2B). The particle size of CR-NPs is smaller than that of AS-ZMNPs (without water evaporation cross-linking), indicating that the water evaporation cross-linking method contributes to the reduction of the particle size of nanoparticles (Fig. S2). A higher intensity cross-linking between MCP and zein possibly occurred during the water evaporation cross-linking process, resulting in a denser structure. Transmission electron microscopy (TEM) revealed that CR-NPs revealed homogeneous spherical particles with a smooth surface and particle size was smaller than that observed using DLS (Fig. 2C). This difference is not surprising owing to the sample preparation in TEM owing to dehydration unlike DLS where hydrodynamic diameter is evaluated (Luo et al., 2020). Furthermore, the encapsulation rates of both Cur and Res in CR-NPs

346 were greater than 88% (Fig. 2D), indicating that the NPs prepared from MCP and zein are suitable
347 co-delivery carriers for Cur and Res.

348 FTIR and XRD were used to further verify the encapsulation of Cur and Res by the CR-NPs.
349 As shown in Fig. 2E, MCP and zein show the characteristic absorption peaks of polysaccharides
350 and proteins respectively such as the stretching vibration of the hydroxyl group (OH) at 3417 cm^{-1},
351 the stretching vibration of the amino group (NH) at 3309 cm^{-1}, the stretching vibration of the
352 carbonyl group (C=O) at 1606 cm^{-1}, the stretching vibration of the amide I and amide II at 1650 cm^{-1}
353 and 1540 cm^{-1}, and the symmetric stretching vibration of the carbonyl group at 1405 cm^{-1} (Zhang
354 et al., 2021). Generally, Cur shows the distinctive absorption peaks at 3507, 1511, 1276, 1205, 1155,
355 1033, and 958 cm^{-1}, which are attributed to hydroxyl (OH) stretching vibrations, ketone (C=O)
356 stretching vibrations, characteristic absorption peaks of benzene rings, and carbon-carbon double
357 bond (C=C) stretching vibrations in the molecular structure of curcumin (Roy & Rhim, 2020). Res
358 exhibits characteristic peaks at 3210, 1438-1589, 1376, 1144, and 968 cm^{-1}, which are attributed to
359 the functional groups of resveratrol (*e.g.*, phenolic hydroxyl group, benzene ring, carbon-carbon
360 double bond) (Qin et al., 2020). However, the characteristic absorption peaks of the phenolic
361 hydroxyl and benzene rings of Cur and Res disappeared in the CR-NPs, suggesting that hydrogen
362 bonding and hydrophobic interaction forces may have occurred between these bioactives and the
363 MCP/zein NPs. The characteristic absorption peaks of Cur and Res at 827-1388 cm^{-1} almost
364 completely disappeared, therefore indicating their successful encapsulation within the NPs.

365 Similar results can also be observed in the XRD pattern (Fig. 2F). Cur and Res exhibit distinct

366 crystalline structures, which is one of the reasons for their poor water solubilities (Guo et al., 2021).
367 Zein also has a more obvious crystalline structure compared to MCP. In contrast, after the formation
368 of CR-NPs, no diffraction peaks of these crystalline structures were observed in the CR-NPs,
369 suggesting that the MCP/Zein NPs showed good co-embedding effect on Cur and Res, with the
370 encapsulated bioactives being present in an amorphous form. The altered crystalline structures of
371 Cur and Res also indicate the existence of interaction forces between them and NPs.

372 *3.3 In vitro digestibility of CR-NPs*

373 The stability of CR-NPs in the gastrointestinal environment is critical for colonic targeted
374 delivery systems to reduce premature leakage of encapsulated drugs (Feng et al., 2020). Zein is a
375 plant protein and is thus responsive to digestive enzymes such as pepsin and trypsin in the
376 gastrointestinal regimes and thus one might expect solely zein-based nanoparticles will not be
377 relevant to allow colon-delivery of bioactives. Although surface coating of zein with MCP may
378 increase its gastrointestinal stability just as observed in other protein nanoparticle-polysaccharide
379 systems (Sarkar et al., 2018), there is still a risk of digestion. Here is where the uniqueness of CR-
380 NPs lies as this is prepared *via* a combined antisolvent precipitation method and water evaporation-
381 induced cross-linking which converts crystalline Cur and Res into amorphous and fuses them within
382 this nano-delivery vehicle with high gastrointestinal stability. Compared to sole zein NPs and the
383 AS-ZMNPs prepared by antisolvent precipitation (without the water-evaporation-based additional
384 crosslinking step), CR-NPs demonstrated significantly lower digestibility (Fig. 3A), suggesting that
385 CR-NPs are a more suitable nano-delivery system for colonic delivery of drugs and nanomedicines.

386 Subsequently, the digested samples were analyzed by SDS-PAGE (Fig. 3B). The results showed that
387 both zein NPs and AS-ZMNPs were significantly degraded compared to pure zein, whilst
388 unprecedented results for the SDS-PAGE clearly demonstrates the outstanding ability of CR-NPs to
389 survive in the gastric and intestinal digestion stages with clear zein bands. The results shown the
390 limited changes of CR-NPs after gastric and intestinal digestion, which further confirms the lack of
391 structural changes and the excellent stability of CR-NPs in the gastrointestinal environment, often
392 not achieved by protein-polysaccharide-based nanodelivery vehicles, mainly owing to the continued
393 water evaporation step creating the crosslinking and stability.

394 *3.4 In vitro release profile of CR-NPs*

395 The release behavior of drugs is an important evaluation indicator for nano-delivery systems.
396 The slow release of drugs usually increases efficacy and reduces drug-associated side effects. As
397 shown in Fig. 3C, the release of Cur and Res in simulated gastric juice (pH 2) at 2 h was low and
398 the release of Cur was greater than that of Res. After a subsequent exposure to simulated intestinal
399 fluid environment (pH 7.2) at 4 h, the overall release of Cur and Res was 29.78% and 29.11%,
400 respectively. The release behavior of Cur and Res differed slightly between the two phases, with
401 Cur first being released rapidly in the gastric juice and the release remaining stable thereafter. A
402 similar behavior was observed in the intestinal fluid, but the overall release was greater in the
403 intestinal fluid than in the gastric fluid. Res, on the other hand, exhibited a sustained release behavior
404 in the intestinal fluid, with a smaller burst release rate than Cur and an obvious greater release in the
405 intestinal fluid than in the gastric fluid. These differences may be related to differences in the

406 molecular structure of Res and Cur, as well as to the interaction forces with the nanoparticles, or
407 possibly to competitive release behavior between Cur and Res. Overall, CR-NPs enabled limited
408 and also controlled release of Cur and Res particularly in the gastrointestinal environment.

409 *3.5 Interactions analysis of CR-NPs*

410 Subsequently, the interaction forces between NPs, curcumin and resveratrol were probed
411 using molecular docking techniques. The process of nanoparticle formation is illustrated in Fig. 3D,
412 where Cur and Res are co-encapsulated inside the hydrophobic cavity and MCP is cross-linked on
413 the surface of the particle. The results showed that hydrogen bonding and hydrophobic interaction
414 forces were the main interaction forces between MCP/zein NPs, Cur and Res during the formation
415 of the CR-NPs (Fig. 3E). Specifically, there are van der Waals forces, Pi-Pi stacked, and Pi-Alkyl
416 between Res and the MCP/zein NPs, whereas the interaction forces between Cur and the NPs are
417 van der Waals forces, Pi-sigma, carbon-hydrogen bonding, and Pi-Alkyl, which are closely related
418 to the structure of both (Fig. 3F). The larger molecular weight of Cur compared to that of Res
419 resulted in greater spatial hindrance and stronger interactions force, which may account for the
420 different encapsulation rate and release behavior of Cur compared to Res. These results are in
421 agreement with the above FTIR and XRD results.

422 *3.6 In vivo therapeutic efficacy of CR-NPs*

423 Although both resveratrol and curcumin have good activity, however, water solubility and
424 stability limit their application in UC (Gowd et al., 2022). The effects of CR-NPs on UC mice were

used to explore the *in vivo* bioactivity of co-delivered curcumin and resveratrol. The intervention process of CR-NPs on DSS-induced UC mice is demonstrated in Fig. 4A. The mice were treated with 3% DSS in their drinking water to induce the development of UC. After the start of modeling, the mice in the model group showed a gradual decrease in body weight especially after the fourth day of modeling, whilst the mice in the control group showed a slight increase in body weight (Fig. 4B). CR-NPs treatment significantly alleviated weight loss in UC mice. The disease activity index (DAI) was obtained by scoring the UC symptoms including weight change, diarrhea, and blood in the stool of the mice. CR-NPs group had a lower DAI index compared to the model group (Fig. 4C). Colonic length was used to reflect the severity of UC and was significantly shorter in the model group compared to the control group, whilst it increased in the CR-NPs treated mice (Fig. 4D). In addition, DSS led to changes in organ indices in mice, with liver and spleen indices significantly higher in the model group than in the control group, both of which decreased after the CR-NPs intervention (Fig. 4E-F). These results suggest that orally delivered colon-targeted CR-NPs are effective in improving adverse symptoms in DSS-induced UC mice. Previous reports have also shown that co-delivery of anti-inflammatory drugs can effectively reduce the problems of extensive metabolism, rapid clearance, and poor absorption of drugs and significantly enhance their therapeutic effects in UC mice (Ahmad et al., 2021).

Histopathology and immunohistochemistry were used to assess the structural and functional effects of CR-NPs on the colonic tissue of UC mice (Fig. 4G). The results of H&E staining showed that after DSS induction, the colonic tissue of the model group was severely damaged, including the

445 destruction of the crypt structure, intestinal mucosal damage, and inflammatory cell infiltration. In
446 contrast, CR-NPs could effectively improve mucosal damage, restore the crypt structure, and reduce
447 intestinal inflammation. MUC-2 is a mucin that forms a mucus barrier that prevents the invasion of
448 harmful substances and microorganisms while protecting mucosal cells from mechanical and
449 chemical irritants (Jixiang Zhang et al., 2020). The expression of MUC-2 was significantly increased
450 after CR-NPs treatment compared to the model group, indicating that CR-NPs could increase the
451 level of mucin and protect the function of intestinal mucosa. AB-PAS staining further demonstrated
452 that CR-NPs could increase the number of cupped cells in colonic tissues, which was the reason for
453 the increase of MUC-2 expression in CR-NPs group. These results suggest that CR-NPs have an
454 excellent protective effect on colonic tissue structure and intestinal mucosal barrier.

455 The effect of CR-NPs treatment on the levels of colonic inflammatory factors and cytokines
456 in UC mice was determined (Fig. 5). Levels of pro-inflammatory factors such as TNF-α, IL-1β, and
457 IL-6 were significantly increased in the model group and down-regulated after treatment with CR-
458 NPs ($p < 0.05$). In contrast, the content of some cytokines that can improve inflammation such as
459 IL-10, IL-22, and TGF-β decreased in the model group and increased in the CR-NPs group. These
460 results suggest that the co-delivered Cur and Res system developed by MCP and zein has good anti-
461 inflammatory activity *in vivo*. These results are similar to previous reports that phytochemicals of
462 natural origin have a favorable ameliorative effect on intestinal inflammation and intestinal tissue
463 damage (Khan et al., 2023).

464 To investigate the effect of CR-NPs on the level of oxidative stress in UC mice, liver oxidative

stress levels (*e.g.*, MDA, SOD, GR, and CAT) were measured. The results showed a significant increase in MDA levels and a significant decrease in SOD, GR, and CAT activities in the model group ($p < 0.01$), suggesting that DSS leads to increased levels of oxidative stress in mice, further promoting the development of intestinal inflammation (Fig. 6A-D). In contrast, the MDA levels decreased significantly after CR-NPs intervention and were comparable to the levels in the control group ($p < 0.01$). The activities of antioxidant enzymes such as SOD, GR, and CAT were also significantly raised compared to the model group ($p < 0.05$). The above results suggest that co-delivery of curcumin and resveratrol can effectively reduce oxidative stress caused by DSS.

In addition, Serum levels of ET and LBP are related to intestinal permeability, and high levels of ET and LBP imply impairment of the intestinal barrier. The content of ET and LBP were measured to assess intestinal permeability and the results showed that intestinal permeability increased after DSS induced (Seethaler et al., 2021), with significant increases in serum levels of ET and LBP ($p < 0.05$) (Fig. 6E-F). In contrast, after CR-NPs treatment, serum ET and LBP levels returned to normal levels, suggesting that CR-NPs were beneficial in improving the intestinal barrier, which was consistent with the MUC-2 levels and AB-PAS staining results.

UC is an immune-mediated disease. Abnormal immune responses not only occur in the gut but dysregulation of T lymphocyte subsets has also been observed in UC mice and patients (Dulic et al., 2020). The effect of CR-NPs intervention on T-lymphocyte subpopulations in DSS-induced UC mice was further determined by flow cytometry. The results showed that $CD4^+$ T lymphocytes as well as the $CD4^+/CD8^+$ ratio decreased in the model group ($p < 0.01$) (Fig. 6G-H), indicating that

DSS treatment leads to a decrease in immune function in mice. In contrast, CR-NPs increased the number of $CD4^+$ T lymphocytes and $CD4^+/CD8^+$ ratio ($p < 0.05$), which were thought to be negatively correlated with the severity of UC (Geng et al., 2023).

3.7 Effect of CR-NPs on intestinal flora

The microbial community in the gut has a good symbiotic relationship with its host and a healthy gut flora is highly beneficial to human health. The results of the Venn diagram showed that the control, model, and CR-NPs groups had 12,005, 8,003, and 8,775 operational taxonomic units (OTUs), respectively, and the number of OTUs shared by the three groups was 609 (Fig. 7A). This suggests that UC leads to a reduction in the number of species of gut microbes, which is alleviated by the CR-NPs treatment. The effect of CR-NPs treatment on alpha-diversity in UC mice was subsequently analyzed. The results showed that Goods coverage index, Simpson index, and Shannon index all decreased in the model group compared to the control group (Fig. 7B). Notably, all of the aforementioned α-diversity indices increased after treatment with CR-NPs. These results suggest that CR-NPs can increase the species number and diversity of gut microbiota in UC mice providing long-term benefits.

Subsequently, the results of the principal components analysis found that the CR-NPs group was closer to the control group indicating that the two had a more similar richness in microflora species composition compared to the model group (Fig. 7C). Further analysis of the differences in species composition was carried out at different taxonomic levels. At the phylum level, the relative abundance of *Bacteroidetes* and *Verrucomicrobia* increased notably in the model group and

505 decreased in the CR-NPs group (Fig. 7D). At the genus level, the abundance of *Shigella*, *Clostridium*,
506 *Sutterella*, *Alistipes*, *Bacteroides*, *Sutterella*, and *Akkermansia* was obviously up-regulated and that
507 of *Parabacteroides*, *Prevotella*, *Ruminococcus*, *Oscillospira*, and *Coprococcus* was down-regulated,
508 while the CR-NPs showed the opposite result (Fig. 7E-F). Of these, *Shigella*, *Clostridium*, and
509 *Sutterella* are considered to be harmful or pathogenic bacteria that are associated with symptoms
510 such as infection and diarrhea. On the other hand, *Ruminococcus*, *Oscillospira,* and *Coprococcus*
511 are considered to be beneficial bacteria for the production of short-chain fatty acids such as
512 propionic acid, acetic acid, and butyric acid (Fang et al., 2022; Lee et al., 2020).

513 LEfSe analysis was used to identify species with significant differences within each group.
514 When the LDA threshold was set to 4, there was still a high number of significantly different species
515 between the groups (Fig. 7G). The main dominant bacteria in the control group are some intestinal
516 dominant bacteria and beneficial bacteria such as *f_S24_7*, *p_Bacyerodetes*, *f_Lactobacillaceae*, and
517 *f_Erysipelotrichaceae*. The dominant bacteria in the model group are some overgrown bacteria or
518 harmful bacteria including *f_Bacteroidaceae*, *p_Verrucomicrobia*, *g_Akkermansia*, and
519 *g_Clostridium*. The differential species of CR-NPs group are *c_Clostridia*, *p_Firmicutes*,
520 *f_Lachnospiraceae*, *g_Odoribacter*, and *g_Turicibacter*, some of which are beneficial bacteria that
521 can produce short-chain fatty acids.

522 As a major metabolite of intestinal flora, short-chain fatty acids contribute greatly to the
523 maintenance of flora balance and human health. The above results found that CR-NPs could increase
524 the abundance of some short-chain fatty acid-producing bacteria, so the effect of CR-NPs on short-

chain fatty acid production was determined. As shown in Fig. 7H, compared to the control group, the levels of total short-chain fatty acids, acetic acid, propionic acid, butyric acid, and pentanoic acid were all significantly reduced in the model group ($p < 0.01$), which was caused by DSS-induced UC disrupting the balance of intestinal flora in healthy mice (Riwes & Reddy, 2020). In the CR-NPs group, the levels of all short-chain fatty acids were significantly increased ($p < 0.05$), indicating that CR-NPs could effectively improve the intestinal flora of UC mice and promote the production of short-chain fatty acids.

3.8 Effects of CR-NPs on serum and fecal metabolism

Serum metabolites and fecal metabolites were analyzed in mice. The raw data were processed by Profinder and data were analyzed using MetaboAnalyst 5.0 (https://www.metaboanalyst.ca). The PCA results of the mouse serum samples are shown in Fig. 8A, where the samples from control, model, and CR-NPs groups were well separated, indicating altered metabolites. Subsequently, OPLS-DA analysis was carried out on the model and CR-NPs groups, and the results showed that the model and CR-NPs groups were separated obviously (Fig. 8B). The results of the permutation test, R^2=0.981, Q^2=0.94, empirical p-values of Q2 and R2 are both less 0.01, indicated that the model was not overfitted. OPLS-DA analysis under positive and negative ions alone displayed similar results (Fig. S3). Subsequently, differential metabolites were screened based on t-test results ($p < 0.05$), fold change values, and VIP values (VIP > 1). Identification was performed by MS-DAIL in combination with HMDB database. Among the major differential metabolites between the CR-NPs group and the model group were docosahexaenoic acid, lysoPC (18:3), lysoPC (18:2),

lysoPC (18:1), L-Cystine, palmitoleic acid, oleic acid, arachidonic acid, cholic acid, taurocholic acid. All endogenous serum differential metabolites are displayed in Table S2. The results of cluster analysis and heatmap showed more similar metabolite variations between CR-NPs and controls compared to the model group (Fig. 8C). The relevant metabolic pathways were further analyzed. As shown in Fig. 8D, glycerophospholipid metabolism, arachidonic acid metabolism, primary bile acid biosynthesis, and biosynthesis of unsaturated fatty acids plays an important role in the development of UC and the intervention of CR-NPs.

Fecal metabolism exhibited similar results to serum metabolism. In the PCA plot, the control, model, and CR-NPs groups were divided into three independent regions (Fig. 8E). The OPLS-DA results also showed good separation of samples from the model and CR-NPs groups (Fig. 8F) with a good fit and high reliable results (R^2=0.974, Q^2=0.898), which was consistent with that under the positive and negative ion model of OPLS -DA results (Fig. S4). However, more differential metabolites were identified in fecal samples than in serum samples (Table S3), with more than 20 metabolites up-regulated and 9 metabolites down-regulated in the model group compared to the control group (Fig. 8G). The related metabolic pathways are primary bile acid biosynthesis, phenylalanine, tyrosine and tryptophan biosynthesis, linoleic acid metabolism, tryptophan metabolism, arachidonic acid metabolism, and tyrosine metabolism (Fig. 8H). Previous reports have shown linoleic acid metabolism, arachidonic acid metabolism, and glycerophospholipids metabolism to be metabolic pathways associated with UC development (Jiang et al., 2021). And linoleic acid and arachidonic acid metabolic pathways play a very important role in the development

565 of inflammation (Tang et al., 2020). In serum metabolism and fecal metabolism, the levels of
566 arachidonic acid and linoleic acid in the model group were higher than those in the control group,
567 which also indicated the occurrence of inflammation. CR-NPs intervention could effectively
568 improve this phenomenon, indicating that CR-NPs treatment could improve inflammation by
569 regulating arachidonic acid and linoleic acid metabolism. Moreover, UC occurs as a result of
570 tryptophan degradation, leading to tryptophan deficiency, which further exacerbates inflammation
571 (Nikolaus et al., 2017). Our results also found that CR-NPs intervention could modulate tryptophan
572 metabolism, which could also alleviate the development of UC.

573 **4. Conclusions**

574 Herein, we fabricated an innovative oral nano-delivery system based on MCP and zein co-
575 embedding curcumin) and resveratrol using antisolvent followed by novel water evaporation-based
576 crosslinking. Such fabrication resulted in the formation of amorphous nanoparticles where the key
577 interactions between the bioactives and the encapsulant were hydrophobic interactions and
578 hydrogen bonding. CR-NPs are ideal co-embedded nanocarriers because of their small particle size
579 and high encapsulation rates for both curcumin and resveratrol. *In vitro* digestion experiments
580 confirmed the outstanding gastrointestinal stability of CR-NPs and low drug release rates in the
581 gastric and small intestinal fractions, thus enabling the delivery of curcumin and resveratrol in larger
582 proportions to the colon. Further investigation of the alleviating effect of CR-NPs on DSS-induced
583 ulcerative colitis revealed that CR-NPs significantly alleviated the symptoms of DSS-induced
584 weight loss, blood in the stool, shortening of the colon, and damage to colonic tissues. Of more

585 importance, CR-NPs may ameliorate intestinal inflammation by modulating immune homeostasis
586 and cytokine expression. CR-NRs had positive effects on oxidative stress levels and intestinal
587 barrier in UC mice. In addition, CR-NRs could maintain the homeostasis of intestinal flora,
588 improving the imbalance of flora caused by UC, and promoting the production of short-chain fatty
589 acids. Furthermore, metabolomics results suggest that CR-NPs intervention can inhibit
590 inflammation and alleviate the development of UC by modulating arachidonic acid, linoleic acid,
591 and tryptophan metabolism. Novel insights from this study provide a promising new nutrition
592 intervention strategy for treatment of UC based on co-delivery of food bioactives using MCP.

593 **Acknowledgments**

594 This work was supported by the National Key Research and Development Program of China
595 (2023YFF1104001-3), and Jiangxi Provincial Natural Science Foundation, China
596 (20232BCD44003).

597 **Conflict of Interest**

598 The authors declare that they have no conflict of interests.

599 **Reference**

600 Aftab, N., & Vieira, A. (2010). Antioxidant activities of curcumin and combinations of this
601 curcuminoid with other phytochemicals. *Phytotherapy Research: An International Journal*
602 *Devoted to Pharmacological and Toxicological Evaluation of Natural Product Derivatives,*
603 *24*(4), 500-502.
604 Ahmad, A., Ansari, M., Kumar, A., Bishnoi, M., Razacd, S., & Khan, R. (2021). Aminocellulose-
605 grafted polycaprolactone-coated core–shell nanoparticles alleviate the severity of ulcerative
606 colitis: a novel adjuvant therapeutic approach. *Biomaterials Science*, 9 (2021) 5868–5883.
607 Anitha, A., Deepagan, V., Rani, V. D., Menon, D., Nair, S., & Jayakumar, R. (2011). Preparation,

608 characterization, *in vitro* drug release and biological studies of curcumin loaded dextran
609 sulphate–chitosan nanoparticles. *Carbohydrate polymers, 84*(3), 1158-1164.
610 Araiza-Calahorra, A., Akhtar, M., & Sarkar, A. (2018). Recent advances in emulsion-based delivery
611 approaches for curcumin: From encapsulation to bioaccessibility. *Trends in Food Science &*
612 *Technology, 71*, 155-169.
613 de Kok, T. M., van Breda, S. G., & Manson, M. M. (2008). Mechanisms of combined action of
614 different chemopreventive dietary compounds: a review. *European journal of nutrition, 47*, 51-
615 59.
616 do Nascimento, R. d. P., da Fonseca Machado, A. P., Galvez, J., Cazarin, C. B. B., & Junior, M. R.
617 M. (2020). Ulcerative colitis: Gut microbiota, immunopathogenesis and application of natural
618 products in animal models. *Life sciences, 258*, 118129.
619 Doublier, J.-L., Garnier, C., Renard, D., & Sanchez, C. (2000). Protein–polysaccharide interactions.
620 *Current opinion in Colloid & interface Science, 5*(3-4), 202-214.
621 Du, L., & Ha, C. (2020). Epidemiology and pathogenesis of ulcerative colitis. *Gastroenterology*
622 *Clinics, 49*(4), 643-654.
623 Dulic, S., Toldi, G., Sava, F., Kovács, L., Molnár, T., Milassin, Á., Farkas, K., Rutka, M., & Balog,
624 A. (2020). Specific T-cell subsets can predict the efficacy of anti-TNF treatment in
625 inflammatory bowel diseases. *Archivum Immunologiae et Therapiae Experimentalis, 68*, 1-10.
626 Esatbeyoglu, T., Huebbe, P., Ernst, I. M., Chin, D., Wagner, A. E., & Rimbach, G. (2012).
627 Curcumin—from molecule to biological function. *Angewandte Chemie International Edition,*
628 *51*(22), 5308-5332.
629 Fang, S., Qin, T., Yu, T., & Zhang, G. (2022). Improvement of the gut microbiota *In vivo* by a short-
630 chain fatty acids-producing strain *Lactococcus garvieae* CF11. *Processes, 10*(3), 604.
631 Feng, K., Wei, Y., Hu, T., Linhardt, R. J., Zong, M., & Wu, H. (2020). Colon-targeted delivery
632 systems for nutraceuticals: A review of current vehicles, evaluation methods and future
633 prospects. *Trends in Food Science & Technology, 102*, 203-222.
634 Feng, T., Gu, Z., & Jin, Z. (2008). Structural studies of an acidic polysaccharide of Mesona blumes
635 gum. *Journal of the Science of Food and Agriculture, 88*(1), 24-34.
636 Geng, B., Ding, X., Li, X., Liu, H., Zhao, W., Gong, H., Tian, Z., & Guo, J. (2023). Peripheral blood
637 T-lymphocyte subsets are potential biomarkers of disease severity and clinical outcomes in
638 patients with ulcerative colitis: a retrospective study. *BMC gastroenterology, 23*(1), 136.
639 Gowd, V., Jori, C., Chaudhary, A. A., Rudayni, H. A., Rashid, S., & Khan, R. (2022). Resveratrol
640 and resveratrol nano-delivery systems in the treatment of inflammatory bowel disease. *The*
641 *Journal of Nutritional Biochemistry, 109*, 109101.
642 Guo, Q., Shu, X., Hu, Y., Su, J., Chen, S., Decker, E. A., & Gao, Y. (2021). Formulated protein-
643 polysaccharide-surfactant ternary complexes for co-encapsulation of curcumin and resveratrol:
644 Characterization, stability and *in vitro* digestibility. *Food hydrocolloids, 111*, 106265.
645 Hu, B., Yu, S., Shi, C., Gu, J., Shao, Y., Chen, Q., Li, Y., & Mezzenga, R. (2020). Amyloid–
646 polyphenol hybrid nanofilaments mitigate colitis and regulate gut microbial dysbiosis. *ACS*
647 *nano, 14*(3), 2760-2776.
648 Jiang, S., Shen, X., Xuan, S., Yang, B., Ruan, Q., Cui, H., Zhao, Z., & Jin, J. (2021). Serum and

colon metabolomics study reveals the anti-ulcerative colitis effect of Croton crassifolius Geisel. *Phytomedicine, 87*, 153570.
Kaplan, G. G. (2015). The global burden of IBD: from 2015 to 2025. *Nature reviews Gastroenterology & hepatology, 12*(12), 720-727.
Khan, R., Jori, C., Ansari, M. M., Ahmad, A., Nadeem, A., Siddiqui, N., & Sultana, S. (2023). α-Terpineol mitigates dextran sulfate sodium-induced colitis in rats by attenuating inflammation and apoptosis. *ACS omega, 8*(32), 29794-29802.
Lee, M.-S., Yoon, J. W., & Tesh, V. L. (2020). recent advances in understanding the pathogenesis of shiga toxin-producing *Shigella* and *Escherichia coli*. *Frontiers in Cellular and Infection Microbiology, 10*, 620703.
Lin, L., Shen, M., Liu, S., Tang, W., Wang, Z., Xie, M., & Xie, J. (2018). An acidic heteropolysaccharide from *Mesona chinensis*: Rheological properties, gelling behavior and texture characteristics. *International journal of biological macromolecules, 107*, 1591-1598.
Liu, F., Ma, D., Luo, X., Zhang, Z., He, L., Gao, Y., & McClements, D. J. (2018). Fabrication and characterization of protein-phenolic conjugate nanoparticles for co-delivery of curcumin and resveratrol. *Food hydrocolloids, 79*, 450-461.
Luo, R., Lin, M., Zhang, C., Shi, J., Zhang, S., Chen, Q., Hu, Y., Zhang, M., Zhang, J., & Gao, F. (2020). Genipin-crosslinked human serum albumin coating using a tannic acid layer for enhanced oral administration of curcumin in the treatment of ulcerative colitis. *Food Chemistry, 330*, 127241.
Ma, Y., Duan, L., Sun, J., Gou, S., Chen, F., Liang, Y., Dai, F., & Xiao, B. (2022). Oral nanotherapeutics based on Antheraea pernyi silk fibroin for synergistic treatment of ulcerative colitis. *Biomaterials, 282*, 121410.
Minekus, M., Alminger, M., Alvito, P., Ballance, S., Bohn, T., Bourlieu, C., Carrière, F., Boutrou, R., Corredig, M., & Dupont, D. (2014). A standardised static *in vitro* digestion method suitable for food–an international consensus. *Food & function, 5*(6), 1113-1124.
Naeem, M., Lee, J., Oshi, M. A., Cao, J., Hlaing, S. P., Im, E., Jung, Y., & Yoo, J.-W. (2020). Colitis-targeted hybrid nanoparticles-in-microparticles system for the treatment of ulcerative colitis. *Acta Biomaterialia, 116*, 368-382.
Nedovic, V., Kalusevic, A., Manojlovic, V., Levic, S., & Bugarski, B. (2011). An overview of encapsulation technologies for food applications. *Procedia food science, 1*, 1806-1815.
Nikolaus, S., Schulte, B., Al-Massad, N., Thieme, F., Schulte, D. M., Bethge, J., Rehman, A., Tran, F., Aden, K., & Häsler, R. (2017). Increased tryptophan metabolism is associated with activity of inflammatory bowel diseases. *Gastroenterology, 153*(6), 1504-1516. e1502.
Nunes, S., Danesi, F., Del Rio, D., & Silva, P. (2018). Resveratrol and inflammatory bowel disease: The evidence so far. *Nutrition research reviews, 31*(1), 85-97.
Pan, J., Shi, Y., Zou, J., Zhang, X., Xin, B., Zhai, B., Guo, D., Sun, J., & Luan, F. (2024). Preparation technologies, structural features, and biological activities of polysaccharides from Mesona chinensis Benth.: A review. *Journal of ethnopharmacology*, 117979.
Perrone, P., Hewage, C. M., Thomson, A. R., Bailey, K., Sadler, I. H., & Fry, S. C. (2002). Patterns of methyl and O-acetyl esterification in spinach pectins: new complexity. *Phytochemistry,*

690 *60*(1), 67-77.
691 Petersen, B. O., Meier, S., Duus, J. Ø., & Clausen, M. H. (2008). Structural characterization of
692 homogalacturonan by NMR spectroscopy—assignment of reference compounds.
693 *Carbohydrate Research, 343*(16), 2830-2833.
694 Qin, L., He, Y., Zhao, X., Zhang, T., Qin, Y., & Du, A. (2020). Preparation, characterization, and *in*
695 *vitro* sustained release profile of resveratrol-loaded silica aerogel. *Molecules, 25*(12), 2752.
696 Riwes, M., & Reddy, P. (2020). *Short chain fatty acids: Postbiotics/metabolites and graft versus*
697 *host disease colitis.* Paper presented at the Seminars in hematology.
698 Roger, O., Kervarec, N., Ratiskol, J., Colliec-Jouault, S., & Chevolot, L. (2004). Structural studies
699 of the main exopolysaccharide produced by the deep-sea bacterium *Alteromonas infernus*.
700 *Carbohydrate Research, 339*(14), 2371-2380.
701 Roy, S., & Rhim, J.-W. (2020). Preparation of antimicrobial and antioxidant gelatin/curcumin
702 composite films for active food packaging application. *Colloids and Surfaces B: Biointerfaces,*
703 *188*, 110761.
704 Sarkar, A., Ademuyiwa, V., Stubley, S., Esa, N. H., Goycoolea, F. M., Qin, X., Gonzalez, F., &
705 Olvera, C. (2018). Pickering emulsions co-stabilized by composite protein/polysaccharide
706 particle-particle interfaces: Impact on *in vitro* gastric stability. *Food hydrocolloids, 84*, 282-
707 291.
708 Seethaler, B., Basrai, M., Neyrinck, A. M., Nazare, J. A., Walter, J., Delzenne, N. M., & Bischoff,
709 S. C. (2021). Biomarkers for assessment of intestinal permeability in clinical practice.
710 *American Journal of Physiology-Gastrointestinal and Liver Physiology, 321*(1), G11-G17.
711 Shakhmatov, E. G., Udoratina, E. V., Atukmaev, K. V., & Makarova, E. N. (2015). Extraction and
712 structural characteristics of pectic polysaccharides from *Abies sibirica L. Carbohydrate*
713 *polymers, 123*, 228-236.
714 Tang, Q., Cang, S., Jiao, J., Rong, W., Xu, H., Bi, K., Li, Q., & Liu, R. (2020). Integrated study of
715 metabolomics and gut metabolic activity from ulcerative colitis to colorectal cancer: The
716 combined action of disordered gut microbiota and linoleic acid metabolic pathway might fuel
717 cancer. *Journal of Chromatography A, 1629*, 461503.
718 Tang, W., Liu, D., Li, Y., Zou, MY., Shao, YC., Yin, JY., & Nie, SP. (2021). Structural characteristics
719 of a highly branched and acetylated pectin from Portulaca oleracea L. *Food hydrocolloids, 116*,
720 106659.
721 Wang, L., Zhang, X., Xia, Y., Zhao, X., Xue, Z., Sui, K., Dong, X., & Wang, D. (2019). Cooking-
722 inspired versatile design of an ultrastrong and tough polysaccharide hydrogel through
723 programmed supramolecular interactions. *Advanced Materials, 31*(41), 1902381.
724 Wang, YX., Yin, JY., Zhang, T., Xin, Y., Huang, XJ., & Nie, SP. (2021). Utilizing relative ordered
725 structure theory to guide polysaccharide purification for structural characterization. *Food*
726 *hydrocolloids, 115*, 106603.
727 Wu, W., Lin, Y., Farag, M. A., Li, Z., & Shao, P. (2023). Dendrobium as a new natural source of
728 bioactive for the prevention and treatment of digestive tract diseases: A comprehensive review
729 with future perspectives. *Phytomedicine*, 154784.
730 Yan, X., Wang, Y., Chen, Y., Xie, J., & Yu, Q. (2021). Effect of roasting duration on the solubility,

731 structure, and IgE-binding capacity of cashew nut proteins. *Innovative Food Science &*
732 *Emerging Technologies, 68*, 102635.
733 Yang, J., Lin, J., Chen, X., Rong, L., Shen, M., Wang, Y., & Xie, J. (2022). *Mesona chinensis*
734 polysaccharide/zein nanoparticles to improve the bioaccesibility and *in vitro* bioactivities of
735 curcumin. *Carbohydrate polymers, 295*, 119875.
736 Yang, J., Lin, J., Zhang, W., Shen, M., Wang, Y., & Xie, J. (2024). Resveratrol-loaded pH-responsive
737 *Mesona chinensis* polysaccharides-zein nanoparticles for effective treatment of ulcerative
738 colitis. *Journal of the Science of Food and Agriculture*.
739 Yang, J., Shen, M., Luo, Y., Wu, T., Chen, X., Wang, Y., & Xie, J. (2021). Advanced applications of
740 chitosan-based hydrogels: From biosensors to intelligent food packaging system. *Trends in*
741 *Food Science & Technology, 110*, 822-832.
742 Yang, J., Shen, M., Wen, H., Luo, Y., Huang, R., Rong, L., & Xie, J. (2020). Recent advance in
743 delivery system and tissue engineering applications of chondroitin sulfate. *Carbohydrate*
744 *polymers, 230*, 115650.
745 Yuan, Y., Ma, M., Xu, Y., & Wang, D. (2022). Surface coating of zein nanoparticles to improve the
746 application of bioactive compounds: A review. *Trends in Food Science & Technology, 120*, 1-
747 15.
748 Zhang, H., Jiang, L., Tong, M., Lu, Y., Ouyang, XK., & Ling, J. (2021). Encapsulation of curcumin
749 using fucoidan stabilized zein nanoparticles: Preparation, characterization, and *in vitro* release
750 performance. *Journal of Molecular Liquids, 329*, 115586.
751 Zhang, J., Lei, H., Hu, X., & Dong, W. (2020). Hesperetin ameliorates DSS-induced colitis by
752 maintaining the epithelial barrier via blocking RIPK3/MLKL necroptosis signaling. *European*
753 *Journal of Pharmacology, 873*, 172992.
754 Zhang, J., Zhang, X., Wang, Q., & Wu, C. (2023). Changes of physicochemical properties and
755 bioactivities of resveratrol-loaded core-shell biopolymer nanoparticles during *in vitro*
756 gastrointestinal digestion. *Food Chemistry*, 136444.
757 Zhu, M., Huang, R., Wen, P., Song, Y., He, B., Tan, J., Hao, H., & Wang, H. (2021). Structural
758 characterization and immunological activity of pectin polysaccharide from kiwano (*Cucumis*
759 *metuliferus*) peels. *Carbohydrate polymers, 254*, 117371.

760

Credit Author Statement

Jun Yang：Writing-Original Draft, Visualization, Data Curation

Xianxiang Chen: Method

Jieqiong Lin: Writing – Review & Editing

Mingyue Shen: Writing – Review & Editing

Yuanxing Wang: Writing – Review & Editing

Anwesha Sarkar: Writing – Review & Editing

Huiliang Wen: Writing – Review & Editing

Jianhua Xie: Validation, Resources, Supervision

Conflict of Interest

The authors declare that they have no conflict of interests.

Figure captions:

Fig. 1 Structural characterization of MCP. (A) HPGPC spectra of MCP with insets of molecular weight (*Mw*). (B) Monosaccharide composition, where a-j represented Fuc, Rha, Ara, Gal, Glc, Xyl, Man, Fru, GalA, and GlcA, respectively. (C) 1H NMR spectrum of MCP. (D) COSY spectrum. (E) HSQC spectrum. (F) HMBC spectrum, where GA1, GA2, R1, R2, G1, and G2 represented α- (1, 4)-D-GalpA, α-(1, 2, 4)-D-GalpA, α-(1, 2, 4)-L-Rhap, α-(1, 2)-L-Rhap, β-D-Galp, and β-D-Glcp, respectively.

Fig. 2 Preparation and characterization of CR-NPs. (A) Particle size distribution of CR-NPs with inset of mean hydrodynamic diameter. (B) Mean zeta potential of CR-NPs. (C) Transmission electron micrograph of CR-NPs, scale bar = 200 nm. (D) Encapsulation rate of CR-NPs for curcumin (Cur) and resveratrol (Res). (E) FTIR profiles of Res, Cur, zein, *Mesona chinensis* polysaccharides (MCP), and CR-NPs. (D) XRD profiles of Res, Cur, zein, MCP, and CR-NPs. Data are mean ± SD. (n = 3).

Fig. 3 *In vitro* digestibility, release, and interaction of CR-NPs. (A) Content of soluble peptides after *in vitro* digestion. (B) SDS-PAGE electrophogram after digestion, where a-j are marker, Zein, Gastric digested zein NPs, gastric digested AS-ZMNPs, gastric digested CR-NPs, intestinal digested Zein NPs, intestinal digested AS-ZMNPs, intestinal digested CR-NPs, Pepsin, Trypsin respectively. (C) *In vitro* release behavior of Cur and Res from CR-NPs. (D) Schematic representation of nanoparticles formation. (E) and (F) Interaction analysis of MCP/zein NPs, Cur, and Res in molecular docking results. Data are mean ± SD (n = 3, $*p < 0.05$).

Fig. 4 *In vivo* therapeutic effect of CR-NPs against UC. (A) Experimental illustration of the CR-NPs against UC. (B) Weight change. (C) Disease Activity Index. (D) Colonic length. (E) Liver Index. (F) Spleen Index. (G) H&E staining, AB-PAS staining, and MUC-2 expression. Control is healthy mice, model is 3% DSS-induced UC, and positive is ASA treatment. Data are expressed as mean ± SD (n = 6, $*p < 0.05$, $**p < 0.01$).

Fig. 5 Effect of CR-NPs on inflammation in UC mice. Expression of TNF-α, IL-1β, IL-6, IL-10, IL-22, and TGF-β in mouse colon tissue, Data are expressed as mean ± SD (n = 6, $*p < 0.05$, $**p < 0.01$). Expression of F4/80, CD4, CD8, and CD25 in the mouse colon (n = 3). Control is healthy mice, model is 3% DSS-induced UC, and positive is ASA treatment.

Fig. 6 Effects of CR-NPs on oxidative stress, intestinal barrier and immunity in UC mice. Liver oxidative stress levels in mice, the content of (A) malondialdehyde (MDA), (B) superoxide dismutase (SOD), (C) Glutathione reductase (GR), (D) Catalase (CAT), Data are expressed as mean ± SD (n = 6, $*p < 0.05$, $**p < 0.01$). Serum levels of (E) LBP and (F) ET. Splenic lymphocyte subsets, (G) $CD4^+$ and (H) $CD4^+/CD8^+$ ratios, data are mean ± SD (n = 3, $*p < 0.05$ and $**p < 0.01$). Control is healthy mice, model is 3% DSS-induced UC, and positive is ASA treatment.

Fig. 7 Effect of CR-NPs on intestinal flora and short-chain fatty acids. (A) Venn diagram. (B)

α-diversity. (C) Principal component analysis. (D) Species composition at the phylum level. (E) Differences in species composition between groups. (F) Heat map analysis of species composition at the genus level. (G) LEfSe analysis (LDA threshold = 4), n = 5. (H) Effects of CR-NPs on the production of short-chain fatty acids. Control is healthy mice, model is 3% DSS-induced UC, and positive is ASA treatment. Data are expressed as mean ± SD (n = 6, $*p < 0.05$, $**p < 0.01$).

Fig. 8 Effect of CR-NPs on serum and fecal metabolism. (A) Principal component analysis (PCA) plot of serum metabolites. (B) Orthogonal partial least squares discrimination analysis (OPLS-DA) plot of serum metabolites, R^2=0.981, Q^2=0.94. (C) Heat map of serum metabolites. (D) Pathways analysis in serum. (E) PCA plot of fecal metabolites. (F) OPLS-DA plot of fecal metabolites, R^2=0.974, Q^2=0.898. (G) Heat map of fecal metabolites. (H) Pathways analysis in fecal.

Fig. 1

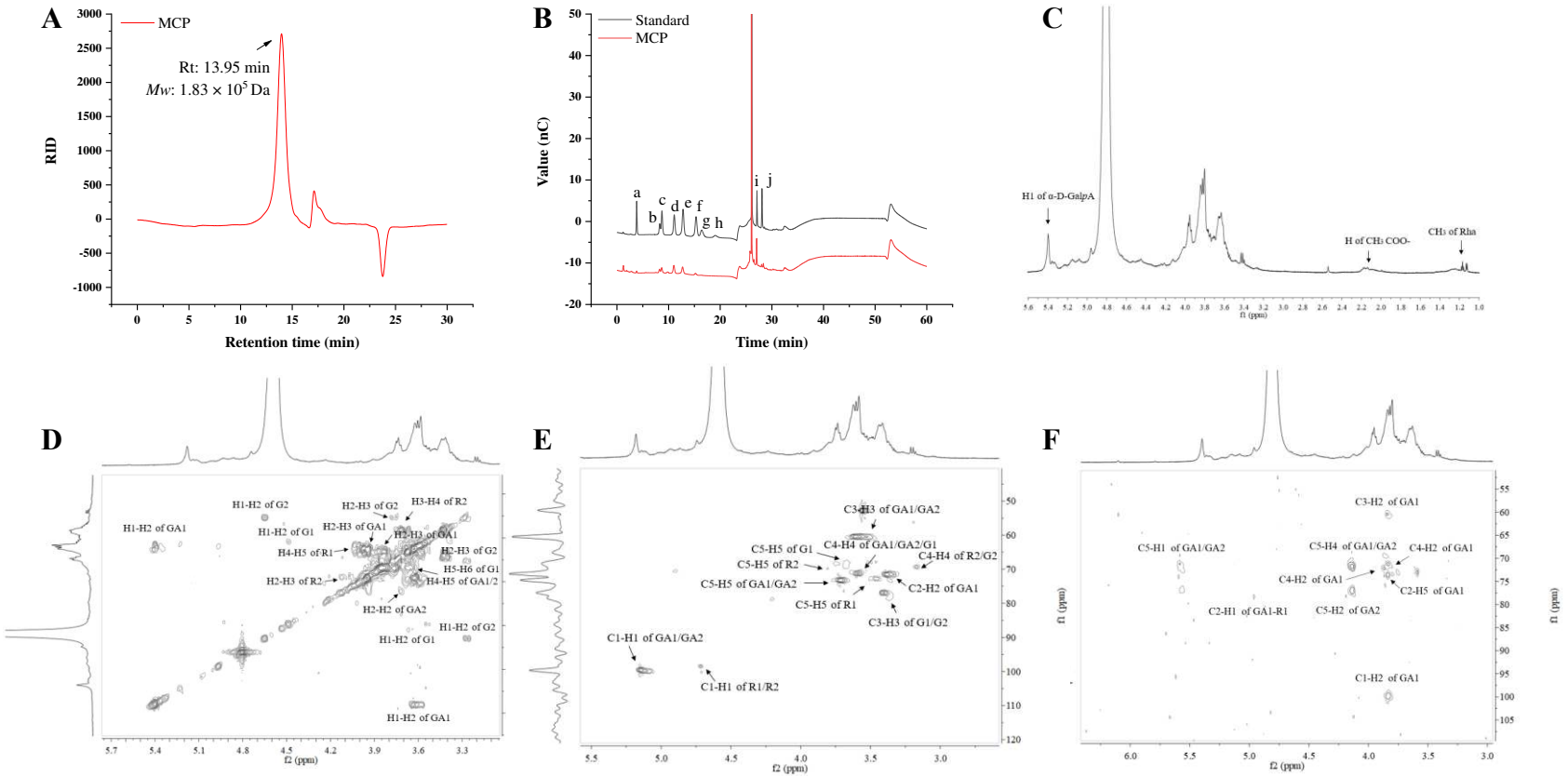
A
MCP
Rt: 13.95 min
Mw: 1.83 × 10^5 Da
RID
Retention time (min)
B
Standard
MCP
Value (nC)
a
b
c
d
e
f
g
h
i
j
Time (min)
C
H1 of α-D-GalpA
H of CH3 COO-
CH3 of Rha
f1 (ppm)
D
H1-H2 of G2
H2-H3 of G2
H3-H4 of R2
H1-H2 of GA1
H1-H2 of G1
H2-H3 of GA1
H2-H3 of GA1
H4-H5 of R1
H2-H3 of G2
H5-H6 of G1
H2-H3 of R2
H4-H5 of GA1/2
H2-H2 of GA2
H1-H2 of G2
H1-H2 of G1
H1-H2 of GA1
f2 (ppm)
E
C3-H3 of GA1/GA2
C5-H5 of G1
C4-H4 of GA1/GA2/G1
C5-H5 of R2
C4-H4 of R2/G2
C5-H5 of GA1/GA2
C2-H2 of GA1
C5-H5 of R1
C3-H3 of G1/G2
C1-H1 of GA1/GA2
C1-H1 of R1/R2
f2 (ppm)
F
C3-H2 of GA1
C5-H1 of GA1/GA2
C5-H4 of GA1/GA2
C4-H2 of GA1
C4-H2 of GA1
C2-H5 of GA1
C2-H1 of GA1-R1
C5-H2 of GA2
C1-H2 of GA1
f2 (ppm)
f1 (ppm)

829 **Fig. 2**

830

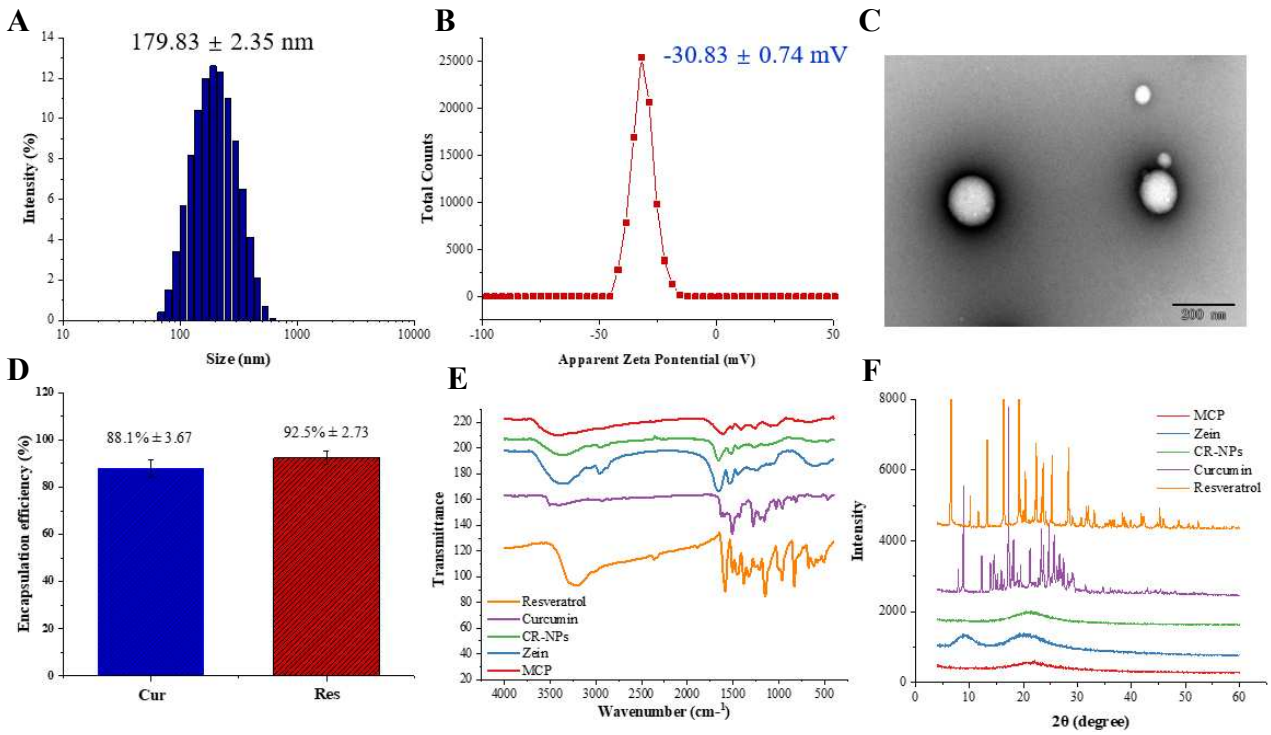

831

832

833

834 **Fig. 3**

835

836

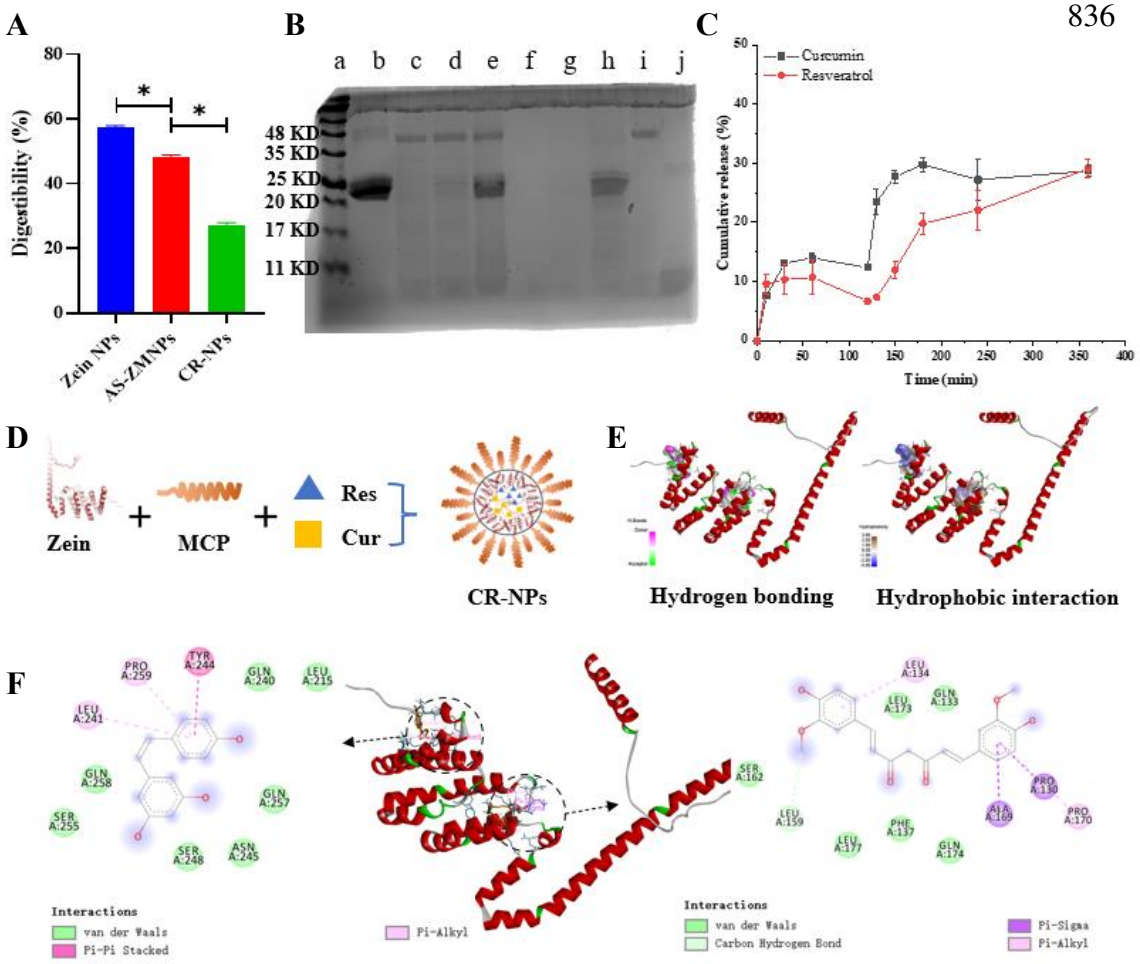

838 **Fig. 4**

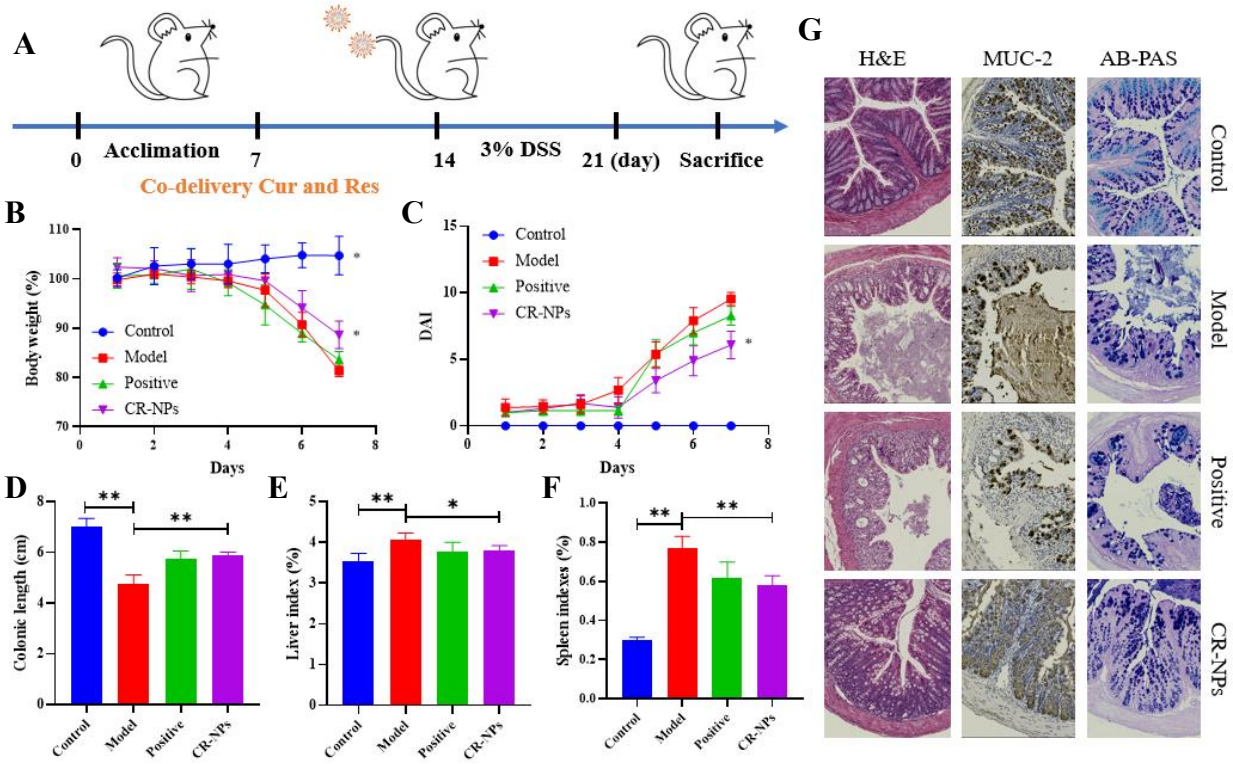
A
0
Acclimation
7
14
3% DSS
21 (day)
Sacrifice
Co-delivery Cur and Res
B
Bodyweight (%)
Days
Control
Model
Positive
CR-NPs
C
DAI
Days
D
Colonic length (cm)
E
Liver index (%)
F
Spleen indexes (%)
G
H&E
MUC-2
AB-PAS
Control
Model
Positive
CR-NPs

839

840 **Fig. 5**

841

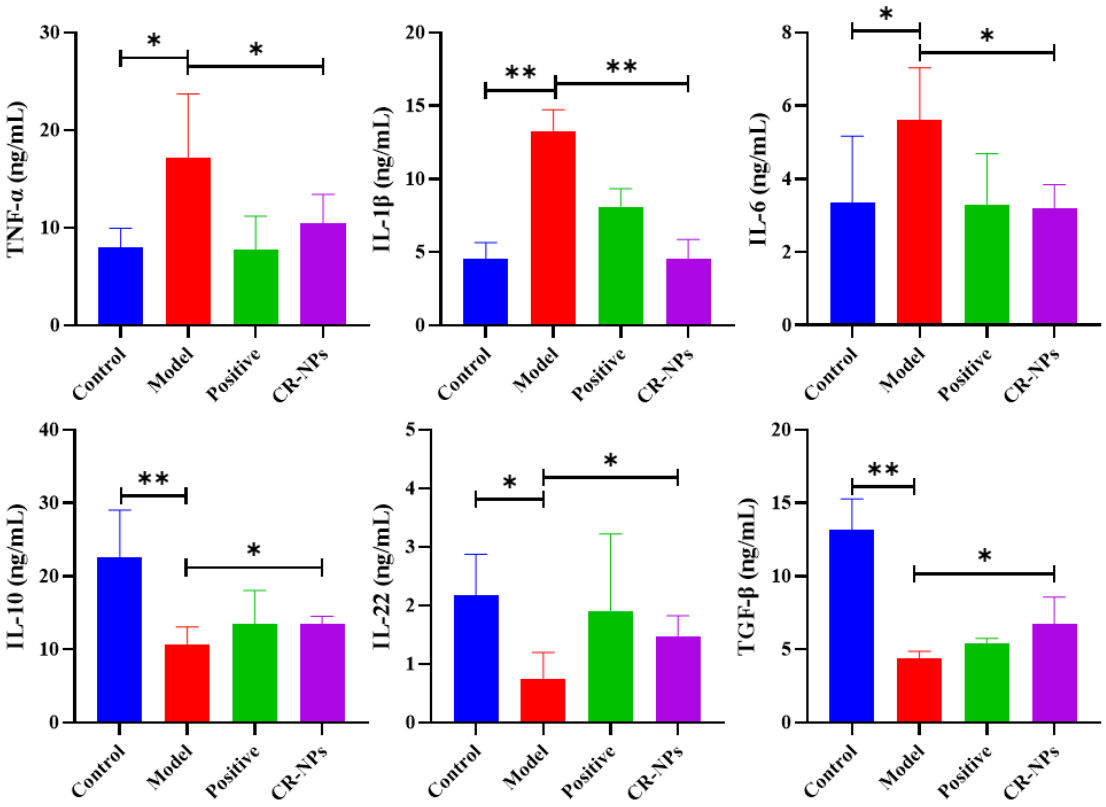
TNF-α (ng/mL)
IL-1β (ng/mL)
IL-6 (ng/mL)
IL-10 (ng/mL)
IL-22 (ng/mL)
TGF-β (ng/mL)
Control
Model
Positive
CR-NPs

842 **Fig. 6**

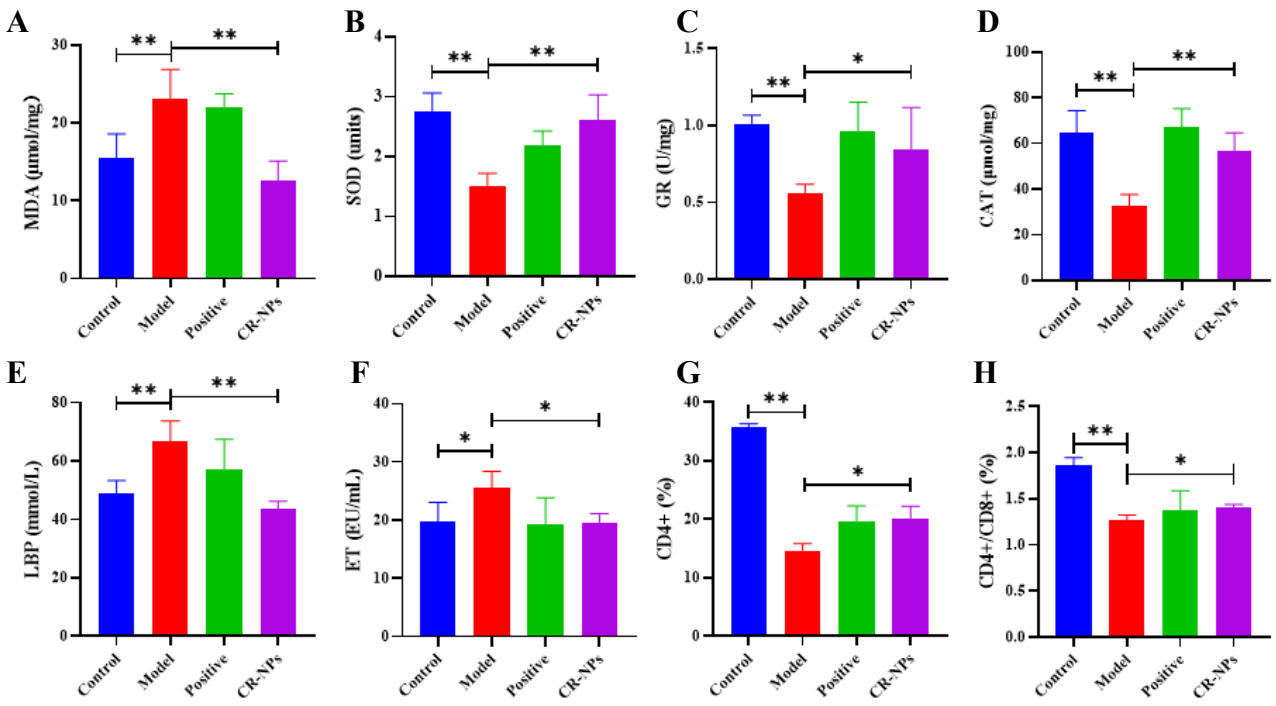
A
MDA (μmol/mg)
B
SOD (units)
C
GR (U/mg)
D
CAT (μmol/mg)
E
LBP (mmol/L)
F
ET (EU/mL)
G
CD4+ (%)
H
CD4+/CD8+ (%)
Control
Model
Positive
CR-NPs

843

844 **Fig. 7**

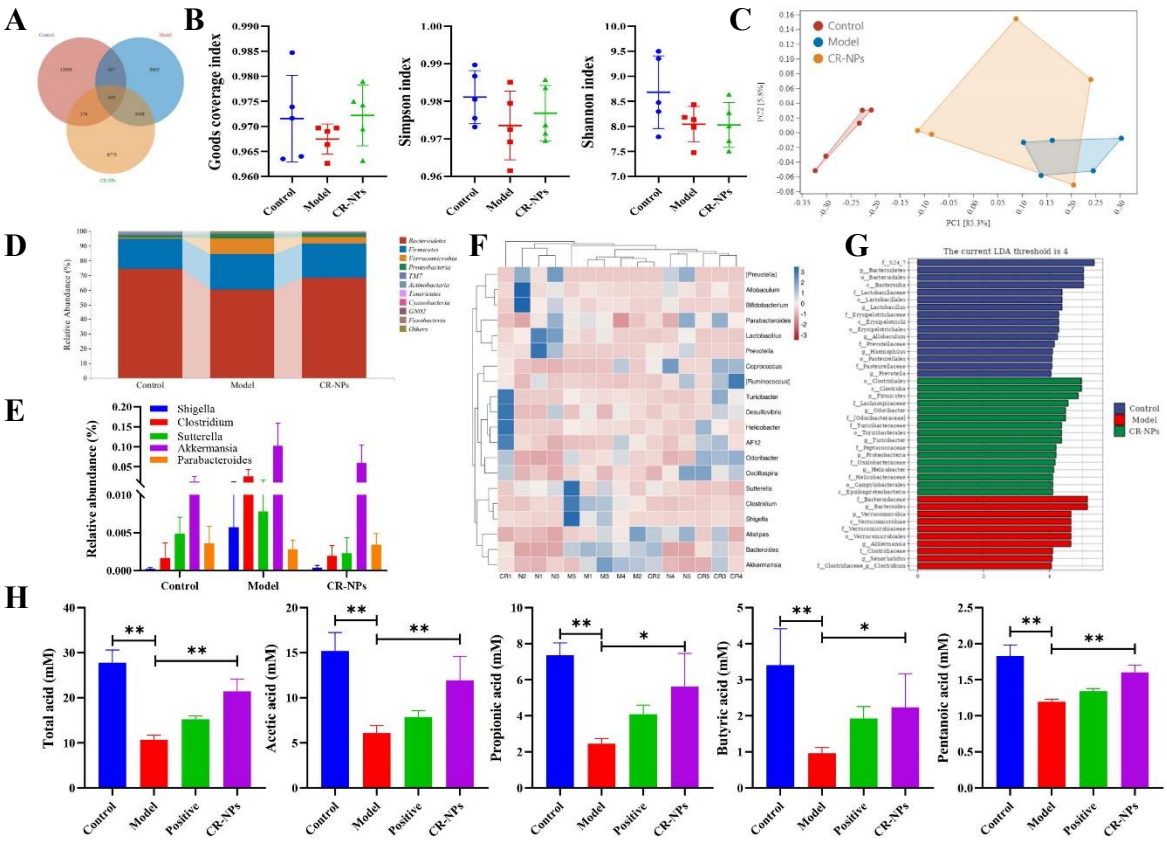

845

846

847 **Fig. 8**

848

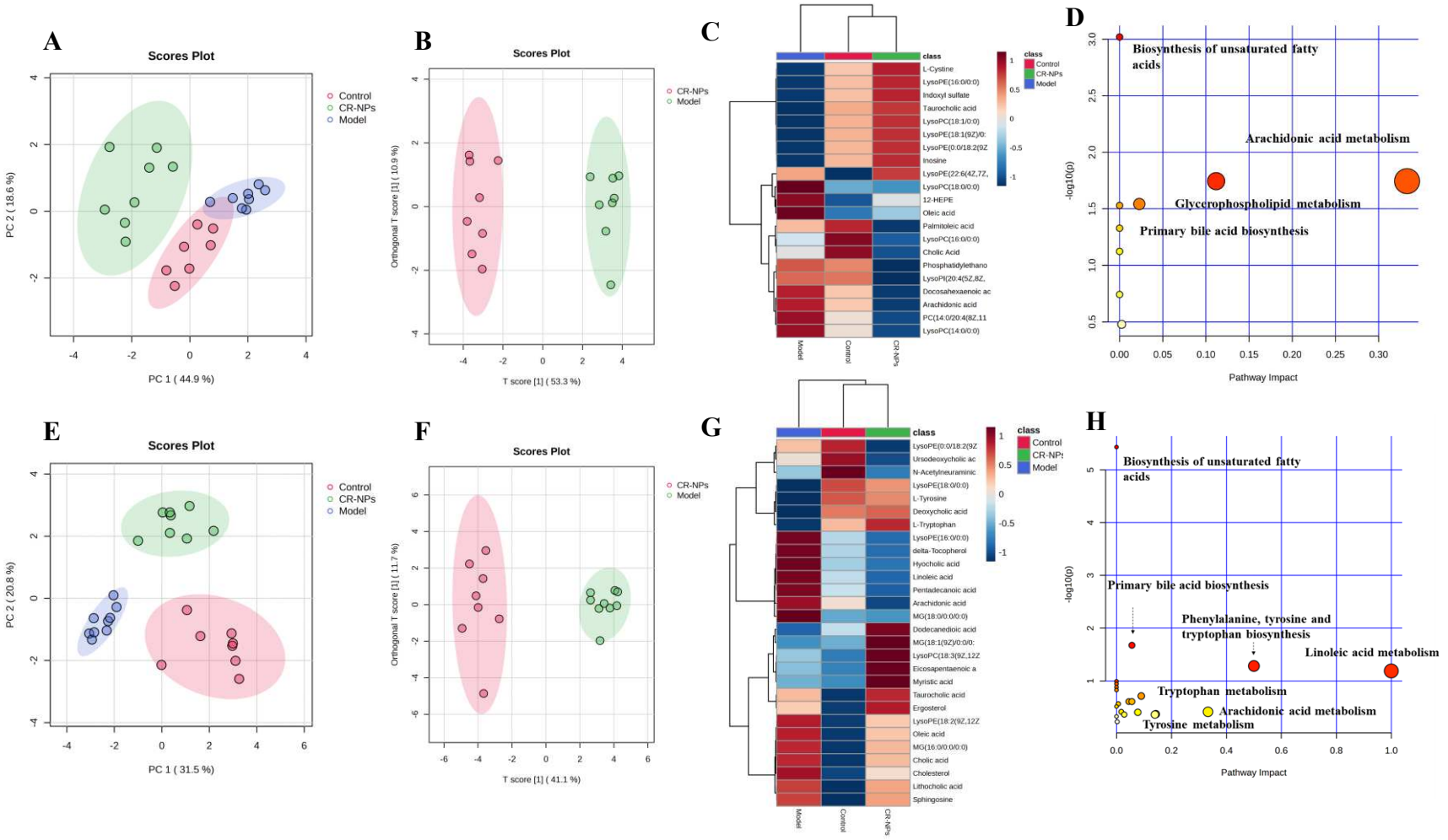
A
Scores Plot
Control
CR-NPs
Model
PC 2 (18.6 %)
PC 1 (44.9 %)
B
Scores Plot
CR-NPs
Model
Orthogonal T score [1] (10.9 %)
T score [1] (53.3 %)
C
class
Control
CR-NPs
Model
L-Cystine
LysoPE(16:0/0:0)
Indoxyl sulfate
Taurocholic acid
LysoPC(18:1/0:0)
LysoPE(18:1(9Z)/0:
LysoPE(0:0/18:2(9Z
Inosine
LysoPE(22:6(4Z,7Z,
LysoPC(18:0/0:0)
12-HEPE
Oleic acid
Palmitoleic acid
LysoPC(16:0/0:0)
Cholic Acid
Phosphatidylethano
LysoPI(20:4(5Z,8Z,
Docosahexaenoic ac
Arachidonic acid
PC(14:0/20:4(8Z,11
LysoPC(14:0/0:0)
D
Biosynthesis of unsaturated fatty acids
Arachidonic acid metabolism
Glycerophospholipid metabolism
Primary bile acid biosynthesis
-log10(p)
Pathway Impact
E
Scores Plot
Control
CR-NPs
Model
PC 2 (20.8 %)
PC 1 (31.5 %)
F
Scores Plot
CR-NPs
Model
Orthogonal T score [1] (11.7 %)
T score [1] (41.1 %)
G
class
Control
CR-NPs
Model
LysoPE(0:0/18:2(9Z
Ursodeoxycholic ac
N-Acetylneuraminic
LysoPE(18:0/0:0)
L-Tyrosine
Deoxycholic acid
L-Tryptophan
LysoPE(16:0/0:0)
delta-Tocopherol
Hyocholic acid
Linoleic acid
Pentadecanoic acid
Arachidonic acid
MG(18:0/0:0/0:0)
Dodecanedioic acid
MG(18:1(9Z)/0:0/0:
LysoPC(18:3(9Z,12Z
Eicosapentaenoic a
Myristic acid
Taurocholic acid
Ergosterol
LysoPE(18:2(9Z,12Z
Oleic acid
MG(16:0/0:0/0:0)
Cholic acid
Cholesterol
Lithocholic acid
Sphingosine
H
Biosynthesis of unsaturated fatty acids
Primary bile acid biosynthesis
Phenylalanine, tyrosine and tryptophan biosynthesis
Linoleic acid metabolism
Tryptophan metabolism
Arachidonic acid metabolism
Tyrosine metabolism
-log10(p)
Pathway Impact

Table S1 The possible ^{1}H and ^{13}C NMR assignments of MCP

	Glycosidic linkages	H1/C1	H2/C2	H3/C3	H4/C4	H5/C5	H6/C6
GA1	α-(1, 4)-D-GalpA	5.39/99.97	3.65/71.82	3.8/60.59	3.84/71.6	3.96/73.21	--
GA2	α-(1, 2, 4)-D-GalpA	5.33/99.76	3.95/78.23	3.82/60.18	3.85/71.2	3.96/73.01	--
R1	α-(1, 2, 4)-L-Rhap	4.96/98.21	3.98/76.8	4.02	3.92	3.69/72.8	1.16
R2	α-(1, 2)-L-Rhap	5.14/98.78	4.12	3.76	3.4/69.64	4.01/68.25	1.12
G1	β-D-Galp	4.45	3.58	3.63	3.84	3.97	3.55
G2	β-D-Glcp	4.65	3.26	3.54/77.51	3.39/68.87	3.82	3.59

able S2 Endogenous differential metabolites in mouse serum samples.

m/z	RT (min)	Metabolites	HMDB ID	P Value	VIP	Log2FC(CR-NPs/M)	Adduct
330.273	22.89	Docosahexaenoic acid	HMDB0002183	3.49E-07	1.12	1.14	[M+H]+
519.33	14.17	LysoPC(18:3/0:0)	HMDB0010387	1.54E-09	1.19	-6.66	[M+H]+
519.332	15.84	LysoPC(18:2/0:0)	HMDB0010386	5.48E-07	1.12	0.42	[M+H]+
521.344	15.85	LysoPC(18:1/0:0)	HMDB0002815	4.93E-09	1.18	0.94	[M+H]+
213.847	1.24	Indoxyl sulfate	HMDB0000682	2.79E-06	1.51	0.43	[M-H]-
239.939	1.17	L-Cystine	HMDB0000192	6.85E-04	1.28	0.71	[M-H]-
252.137	19.07	Palmitoleic acid	HMDB0003229	2.47E-10	1.64	-2.32	[M-H]-
267.813	1.26	Inosine	HMDB0000195	3.94E-05	1.42	0.38	[M-H]-
282.328	26.69	Oleic acid	HMDB0000207	8.26E-03	1.09	-1.50	[M-H]-
304.314	24.98	Arachidonic acid	HMDB0001043	1.31E-02	1.03	-2.59	[M-H]-
318.222	17.19	12-HEPE	HMDB0010202	8.17E-05	1.41	-1.36	[M-H]-
406.042	1.51	Cholic Acid	HMDB0000619	2.40E-05	1.44	-1.78	[M-H]-
453.937	1.15	LysoPE(16:0/0:0)	HMDB0011503	1.81E-04	1.35	1.06	[M-H]-
477.293	15.17	LysoPE(0:0/18:2)	HMDB0011477	8.45E-03	1.07	-0.38	[M-H]-
481.808	1.19	LysoPE(18:1/0:0)	HMDB0011506	2.28E-03	1.19	0.40	[M-H]-
513.892	1.16	Taurocholic acid	HMDB0000036	5.27E-03	1.12	0.68	[M-H]-
525.294	15.27	LysoPE(22:6/0:0)	HMDB0011526	3.12E-04	1.33	-0.69	[M-H]-
527.309	16.32	LysoPC(14:0/0:0)	HMDB0010379	4.16E-04	1.31	-1.53	[M-H]-
555.362	17.99	LysoPC(16:0/0:0)	HMDB0010382	5.80E-03	1.10	-1.04	[M-H]-
582.471	25.24	LysoPC(18:0/0:0)	HMDB0010384	6.82E-06	1.50	-1.22	[M-H]-
620.306	17.12	LysoPI(20:4/0:0)	HMDB0010395	3.29E-04	1.31	-1.79	[M-H]-
813.559	17.18	PC(14:0/20:4)	HMDB0007884	1.88E-07	1.58	-2.79	[M-H]-

Table S3 Endogenous differential metabolites in mouse fecal samples.

m/z	RT (min)	Metabolites	HMDB ID	P Value	VIP	Log2FC(CR-NPs/M)	Adduct
282.254	17.48	Oleic acid	HMDB0000207	1.45E-03	1.59	-0.80	[M+H]+
294.217	16.14	Isopalmitic acid	HMDB0031068	8.21E-05	1.86	-2.21	[M+H]+
322.245	17.47	Sphingosine	HMDB0000252	4.18E-02	1.10	-0.50	[M+H]+
353.287	18.76	MG(16:0/0:0/0:0)	HMDB0011564	3.27E-02	1.19	-0.78	[M+H]+
378.285	9.57	MG(18:1/0:0/0:0)	HMDB0011567	1.17E-02	1.32	1.18	[M+H]+
381.428	17.76	MG(18:0/0:0/0:0)	HMDB0011131	4.81E-04	1.68	-1.95	[M+H]+
388.259	13.36	Cholesterol	HMDB0000067	4.12E-04	1.73	-0.90	[M+H]+
425.246	13.36	delta-Tocopherol	HMDB0002902	1.01E-02	1.36	-1.08	[M+H]+
430.265	10.5	Ursodeoxycholic acid	HMDB0000946	1.69E-02	1.28	-1.12	[M+H]+
430.299	15.6	Hyocholic acid	HMDB0000760	2.93E-02	1.19	-0.52	[M+H]+
200.139	19.92	Sebacic acid	HMDB0000792	2.25E-04	1.85	-0.77	[M-H]-
204.087	3.07	L-Tryptophan	HMDB0000929	1.87E-02	1.35	0.89	[M-H]-
216.133	8.98	Undecanedioic acid	HMDB0000888	7.13E-05	1.97	-1.38	[M-H]-
218.122	2.27	3-Hydroxysebacic acid	HMDB0000350	3.71E-03	1.57	2.46	[M-H]-
221.089	0.87	N-Acetylmannosamine	HMDB0001129	2.66E-03	1.62	0.76	[M-H]-
228.145	2.91	Myristic acid	HMDB0000806	4.25E-04	1.79	3.19	[M-H]-
230.148	10.11	Dodecanedioic acid	HMDB0000623	4.02E-04	1.80	1.79	[M-H]-
243.142	5.5	Pentadecanoic acid	HMDB0000826	2.74E-02	1.29	-1.07	[M-H]-
267.13	0.9	Inosine	HMDB0000195	5.46E-04	1.78	5.63	[M-H]-
278.124	2.41	gamma-Linolenic acid	HMDB0003073	6.50E-04	1.77	3.90	[M-H]-
294.218	16.5	Linoleic acid	HMDB0000673	1.78E-04	1.88	-2.04	[M-H]-
302.225	18.51	Eicosapentaenoic acid	HMDB0001999	3.96E-02	1.15	1.05	[M-H]-
305.921	24.62	Arachidonic acid	HMDB0001043	3.47E-06	2.09	-2.64	[M-H]-

308.198	14.35	N-Acetylneuraminic acid	HMDB0000230	1.36E-02	1.39	-1.38	[M-H]-
328.094	6.37	Docosahexaenoic acid	HMDB0002183	1.38E-02	1.39	-0.53	[M-H]-
361.118	9.44	L-Tyrosine	HMDB0000158	2.89E-03	1.60	0.73	[M-H]-
375.868	0.77	Lithocholic acid	HMDB0000761	3.12E-04	1.84	-1.06	[M-H]-
392.292	12.05	Deoxycholic Acid	HMDB0000626	3.82E-02	1.23	-0.88	[M-H]-
408.286	11.46	Cholic acid	HMDB0000619	2.30E-02	1.28	-1.17	[M-H]-
441.278	9.75	Folic acid	HMDB0000121	4.04E-03	1.58	5.02	[M-H]-
454.296	9.63	LysoPE(16:0/0:0)	HMDB0011503	3.52E-02	1.20	-0.92	[M-H]-
476.277	9.88	LysoPE(18:2/0:0)	HMDB0011507	1.99E-03	1.67	-1.15	[M-H]-
481.318	17.1	LysoPE(18:0/0:0)	HMDB0011130	4.21E-02	1.17	0.84	[M-H]-
502.324	11	LysoPC(18:3/0:0)	HMDB0010388	5.99E-04	1.79	-0.99	[M-H]-
515.328	5.6	Taurocholic acid	HMDB0000036	4.96E-02	1.15	0.32	[M-H]-

Fig. S1

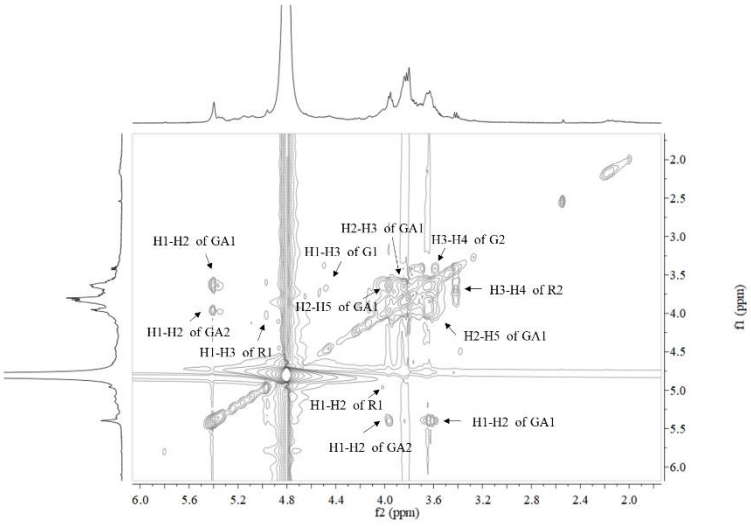

Fig. S1 The TOCSY spectrum of MCP.

Fig. S2

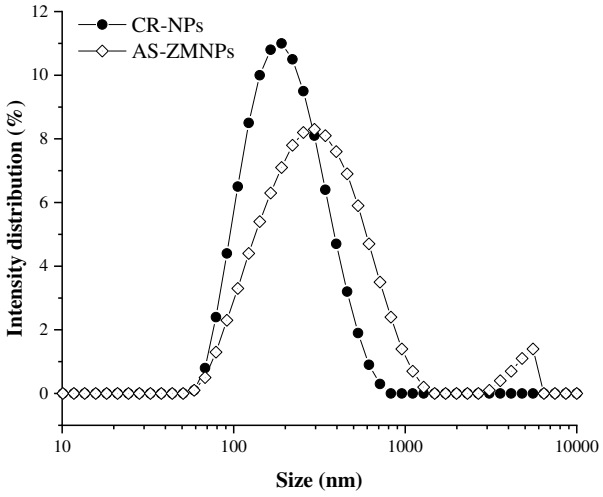

Fig. S2 Particle size distribution of CR-NPs and AS-ZMNPs.

Fig. S3

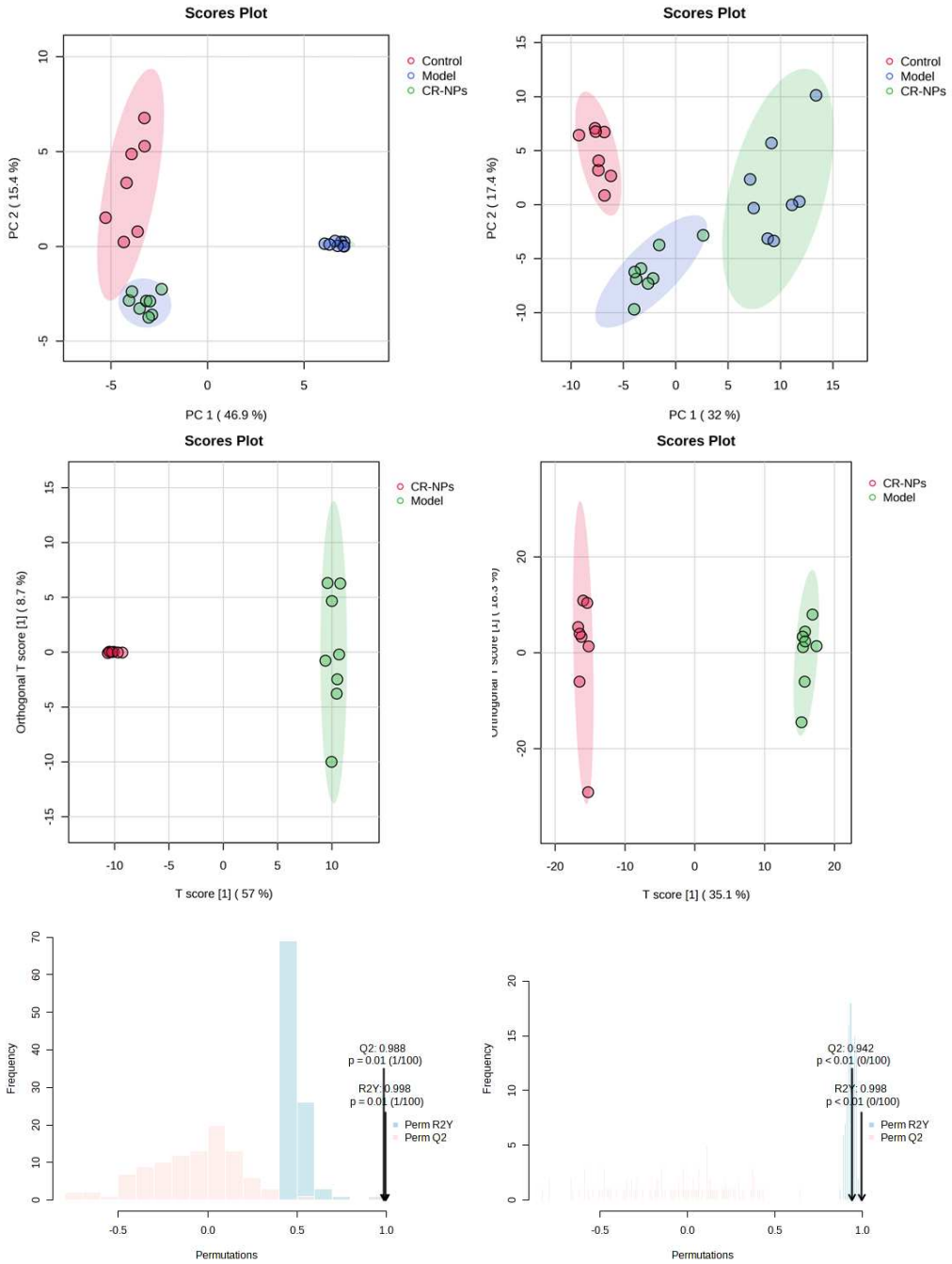

Fig. S3 Multivariate statistical analysis of serum samples. (A) and (B) Principal component analysis (PCA) in the positive and negative ion modes. (C) and (D) Orthogonal partial least squares discrimination analysis (OPLS-DA) in the positive and negative ion modes. (E) and (F) Results of 100 permutation test.

Fig. S4

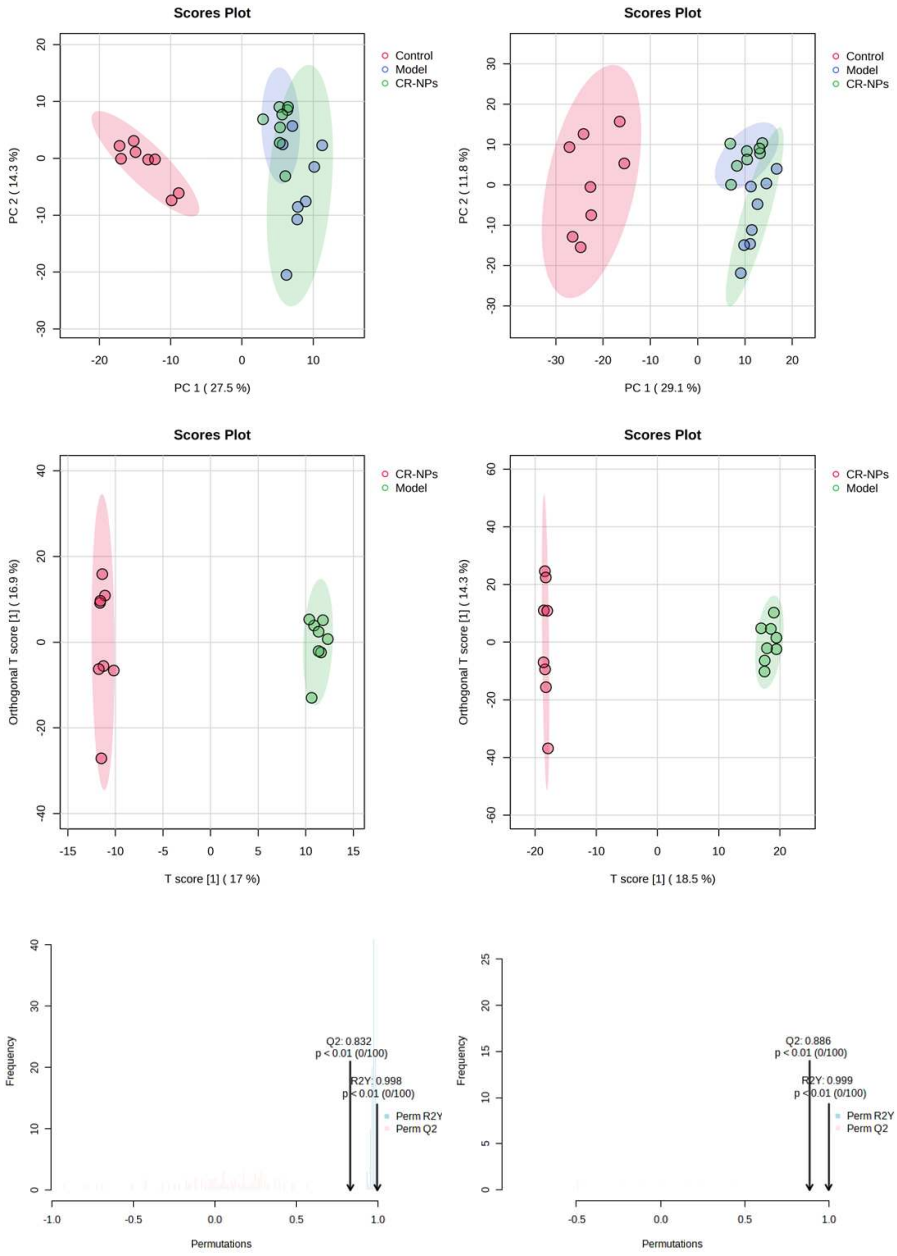

Fig. S4 Multivariate statistical analysis of fecal samples. (A) and (B) Principal component analysis (PCA) in the positive and negative ion modes. (C) and (D) Orthogonal partial least squares discrimination analysis (OPLS-DA) in the positive and negative ion modes. (E) and (F) Results of 100 permutation test.